Two-Phase Modeling of Thermal Frontal Polymerization and Numerical Analysis of Fluid-Motion Effects

Maged A. Faragalla[a,*], Miltiadis V. Papalexandris[a,b]

[a] *Université catholique de Louvain, Institute of Mechanics, Materials and Civil Engineering, 1348, Louvain-la-Neuve, Belgium*
[b] *Walloon Excellence Research Institute, 1300, Wavre, Belgium*

Abstract

Thermal frontal polymerization is a process that converts a liquid monomer solution into a solid polymer through the propagation of a reaction front. This process has gained interest as a fast, energy-efficient method for composite manufacturing. However, it is susceptible to thermoconvective and chemical instabilities that can degrade product quality or even extinguish the entire process. Further, most existing models do not account for fluid convection, which can have an impact on the front dynamics. In this paper, we develop a thermo-mechanical two-phase flow model based on a mixture-theoretic formalism, according to which the liquid reactants and solid polymer are treated as two interacting thermodynamic continua. The model provides a flexible framework for describing reactive solid-fluid systems with both homogeneous and heterogeneous reactions, and explicitly accounts for fluid convection, chemical kinetics, and the exchanges of mass, momentum, and energy between the phases. We also present an algorithm for the numerical treatment of the model, along with validation tests and a numerical study of both stable and unstable front cases. According to our findings, fluid motion does not affect substantially the average front speed but has a noticeable impact on the monomer conversion hence the final composition of the product.

*Corresponding Author

Email addresses: maged.faragalla@uclouvain.be (Maged A. Faragalla), miltiadis.papalexandris@uclouvain.be (Miltiadis V. Papalexandris)

Keywords: frontal polymerization, chemical instabilities, reactive front dynamics, liquid-solid systems, heterogeneous reactions, polymerization kinetics, numerical study

1. Introduction

In this paper, we develop a two-phase flow model for thermal frontal polymerization (TFP) and present numerical simulations that highlight the role of fluid convection in the behavior of the propagating polymerization front. TFP is a self-sustained, exothermic process in which a localized heat source initiates the conversion of a liquid monomer mixture into a solid polymer product through the propagation of a reaction front. Once initiated, the front is maintained by the heat released from the polymerization reaction, enabling rapid and uniform material synthesis with minimal external energy input. This characteristic makes TFP attractive for advanced manufacturing applications such as composite fabrication and additive manufacturing, where energy efficiency and uniform product quality are critical. However, the process is inherently sensitive to chemical and thermoconvective instabilities. These instabilities can modify the front structure and dynamics, affecting the quality of the final polymer or, in severe cases, terminate the reaction process entirely.

One of the earliest studies on TFP was conducted as part of a process discovered by Merzhanov and Borovinskaya [1], known as self-propagating high-temperature synthesis, and subsequently explored by Chechilo et al. [2–5]. Building on these foundations, Pojman and his collaborators combined experimental investigations with mathematical modeling to characterize front speed, stability, and temperature evolution; see, for example, [6–10]. Their contributions established the basis for controlled polymerization with minimal external heating and introduced practical applications of TFP. Theoretical extensions include the model of Solovyov et al. [11] which emphasized the role of chemical kinetics in front stability, and the analytical model of Spade & Volpert [12] which drew analogies with combustion theory to predict the structure of free-radical polymerization waves. Heifetz et al. [13] examined the initiation of fronts under different heating conditions, identifying parameters that govern wave formation. Also, Texier-Picard et al. [14] investigated the role of interfacial tension on the stability of TFP by coupling reaction–diffusion (RD) equations with the Navier–Stokes equations via

convective terms. Through a linear stability analysis, they showed that the interplay between chemical reactions and interfacial tension can lead to instabilities. Interfacial effects were accounted for by imposing jump conditions at the reaction front.

With the advancement of computer technology, numerical studies became increasingly important. For instance, Dumont [15] introduced a novel approach coupling chemical reaction, phase change, and hydrodynamics through the method of characteristics and a fictitious domain method. More recently, Gao et al. [16, 17] combined experiments and multiphysics simulations to investigate TFP in resin–metal composite systems with thermal anisotropy and conductive strips. They also analyzed how orientation and heat exchange influence front shape and velocity. Tiani et al. [18] further highlighted multidimensional effects and showed that layer thickness plays a critical role in sustaining fronts, an aspect not captured in 1D computations. Also, Ivleva & Merzhanov [19] carried out numerical simulations of TFP in cylindrical samples and analyzed the emergence of periodic and chaotic modes.

Finite-element methods have also been applied to TFP. For instance, Goli et al. [20] proposed a homogenized RD model for carbon/dicyclopentadiene composites and used a finite-element method for 1D and 2D studies that were further validated with experiments. Yi et al. [21] applied finite element modeling to acrylamide hydrogel synthesis, highlighting the role of heat conduction and curing kinetics, while Yao et al. [22] extended these methods to simulate frontal curing–based 3D printing of epoxy/carbon fiber composites. Collectively, these studies demonstrate how finite element analysis enables predictive modeling of both material and process-dependent parameters.

Beyond reaction kinetics and heat transfer, recent efforts have considered fluid motion and fillers as additional mechanisms influencing TFP dynamics. Gao et al. [23] showed that convection in low-viscosity resins strongly affects front angle, flow structures, and stability regimes. Lang et al. [24] numerically investigated TFP in bisphenol A diglycidyl ether resins with Fe_3O_4 nanoparticles, revealing how conductive fillers alter front propagation by enhancing heat loss and reducing exothermic energy. Further, Rongy et al. [25] numerically investigated the coupling between autocatalytic reaction fronts and Marangoni-driven convection in free-surface solution layers, revealing complex unsteady dynamics that strongly affect front propagation.

Despite the extensive research efforts devoted to TFP, existing studies rely on single-phase formulations. Those, however, do not directly account for the interactions between the liquid monomer and the solid polymer. As

a result, the understanding of the role of density variations and fluid motion on the front dynamics remains incomplete.

In this work, this gap is bridged through the development of a fully coupled thermo-mechanical two-phase flow model based on a mixture-theoretic framework. According to it, the liquid and solid phases are treated as coexisting, interacting continua. The model incorporates chemical kinetics, mass and heat exchanges between the two phases. Additional fluid convection effects arising, for example, from density changes, are explicitly accounted for. Through numerical simulations, the influence of fluid motion on front speed, temperature distribution, and overall conversion is assessed. This unified approach provides a physically consistent framework for analyzing and predicting the dynamics of TFP, offering new insight into the mechanisms controlling front behavior.

The article is organized as follows. Section 2 presents the derivation of the thermo-mechanical model and its coupling with a reduced chemical kinetics mechanism for TFP. Section 3 provides the final form of the two-phase model and outlines the algorithm that is used for its numerical treatment. In Section 4, the proposed algorithm is tested and validated by comparing results for 1D test cases with earlier numerical results. For the purposes of consistency of comparisons, these tests are based on the reduced RD model (i.e. in absence of fluid motion). Section 5 compares the predictions of the reduced RD model with those of the full model. Finally, Section 6 provides concluding remarks.

2. Mixture-theoretic framework for reacting solid-fluid systems

This section introduces the derivation of the thermo-mechanical model, which incorporates detailed chemical kinetics, variable fluid density, and mass, momentum, and energy exchanges between the two phases. The formulation follows the approach of [26] for flows in mixed porous-pure fluid domains. According to it, the polymer product is represented as a porous medium, i.e. a solid material with voids.

2.1. Conservation laws

The assumptions upon which the present mixture-theoretic formalism is based are the following.

(i) Both phases are treated as immiscible but coexisting continua that completely fill the space they occupy.

(ii) The two phases exchange mass, momentum, and energy with each other. Further, these exchanges are pure; in other words, their sum vanishes.

(iii) The solid medium is assumed to be at rest and with constant density. Whereas the fluid is assumed to be Newtonian and isotropic.

Throughout the article the index s is reserved to denote quantities attributed to the solid phase. In relation to assumption (i), the volume fractions of the two phases $\phi(\boldsymbol{x}, t)$ and $\phi_{\mathrm{s}}(\boldsymbol{x}, t)$ respectively, are introduced as field variables. They take values between 0 and 1 and satisfy the saturation condition $\phi+\phi_{\mathrm{s}} = 1$ everywhere in the domain. The limit case $\phi = 1$ corresponds to a pure fluid phase. While $\phi = 0$ corresponds to a pure solid phase without voids.

With regard to assumption (ii), constitutive relations for the interactions between the two phases are derived by exploiting the entropy inequality for the combined two-phase system [26].

The fluid phase is assumed to consist of r miscible species. Accordingly, the mass, species, momentum, and energy balance laws for the fluid read

$$\frac{\partial \phi\rho}{\partial t} + \nabla\cdot(\phi\rho\boldsymbol{u}) \;=\; \mathcal{M}\,, \tag{1}$$

$$\begin{aligned}\frac{\partial \phi\rho Y_i}{\partial t} + \nabla\cdot(\phi\rho\boldsymbol{u}Y_i) \;&=\; \dot{\omega}_i M_i + \dot{\omega}_i' M_i \\ &\quad - \nabla\cdot(\phi\boldsymbol{J}_i)\,, \qquad i \;=\; 1,\ldots,r-1\,,\end{aligned} \tag{2}$$

$$\frac{\partial \phi\rho\boldsymbol{u}}{\partial t} + \nabla\cdot(\phi\rho\boldsymbol{u}\boldsymbol{u}) + \nabla(\phi p) \;=\; \nabla\cdot(\phi\boldsymbol{\sigma}^{\mathrm{v}}) - \phi\rho\boldsymbol{g} + \boldsymbol{f}\,, \tag{3}$$

$$\frac{\partial \phi\rho e_t}{\partial t} + \nabla\cdot(\phi\boldsymbol{u}(\rho e_t + p)) \;=\; \nabla\cdot(\phi\boldsymbol{\sigma}^{\mathrm{v}}\boldsymbol{u}) - \nabla\cdot(\phi\boldsymbol{q}) - \phi\rho\boldsymbol{g}\cdot\boldsymbol{u} + \mathcal{E}\,. \tag{4}$$

In the above equations, ρ, $\boldsymbol{u} = (u, v, w)$, p, and e_t denote the fluid's density, velocity, pressure, and total energy per unit mass. Further, Y_i stands for the mass fraction of the i-th species. Also, M_i denotes its molar mass, and $\dot{\omega}_i$ and $\dot{\omega}_i'$ denote the rates of change of its molar concentration due to homogeneous and heterogeneous reactions, respectively.

The terms $\mathcal{M}$, $\boldsymbol{f}$, and $\mathcal{E}$ describe interfacial mass, momentum, and energy exchanges, respectively. Here, $\boldsymbol{\sigma}^{\mathrm{v}}$ denotes the viscous stress tensor of the fluid, $\boldsymbol{J}_i$ the diffusion flux of the i-th species, $\boldsymbol{q}$ the conductive heat flux, and $\boldsymbol{g}$ the gravitational acceleration.

The total energy per unit mass, e_t, is the sum of the fluid's internal and kinetic energies,

$$e_t \;=\; e + \frac{1}{2}\boldsymbol{u}\cdot\boldsymbol{u}\,. \tag{5}$$

Further, upon summation of equation (2) over all fluid species, it follows that

$$\sum_{i=1}^{r}\dot{\omega}_i M_i \;=\; 0\,, \qquad \sum_{i=1}^{r}\nabla\cdot(\phi\boldsymbol{J}_i) \;=\; 0\,, \tag{6}$$

and

$$\mathcal{M} \;=\; \sum_{i=1}^{r}\dot{\omega}'_i M_i\,. \tag{7}$$

It is noted that, in view of the previous balance laws, the limit $\phi = 0$ can be singular. For this reason, herein ϕ is assumed to be bounded away from zero.

Equivalently, the solid phase is assumed to consist of n miscible species. Its mass, species, momentum and energy balance laws read

$$\frac{\partial\phi_{\rm s}\rho_{\rm s}}{\partial t} \;=\; -\mathcal{M}\,, \tag{8}$$

$$\frac{\partial\phi_{\rm s}\rho_{\rm s}Y_{{\rm s}i}}{\partial t} \;=\; \dot{\omega}_{{\rm s}i}M_{{\rm s}i} + \dot{\omega}'_{{\rm s}i}M_{{\rm s}i} - \nabla\cdot(\phi_{\rm s}\boldsymbol{J}_{{\rm s}i})\;, \quad i \;=\; 1,\ldots n-1\,, \tag{9}$$

$$\nabla(\phi_{\rm s}p_{\rm s}) \;=\; -\nabla\cdot(\phi_{\rm s}\boldsymbol{\tau}_{\rm s}) - \phi_{\rm s}\rho_{\rm s}\boldsymbol{g} - \boldsymbol{f}\,, \tag{10}$$

$$\frac{\partial\phi_{\rm s}\rho_{\rm s}e_{\rm s}}{\partial t} \;=\; -\nabla\cdot(\phi_{\rm s}\boldsymbol{q}_{\rm s}) - \mathcal{E}\,. \tag{11}$$

In the above equations, $\rho_{\rm s}$, $p_{\rm s}$ and $e_{\rm s}$ represent the density, pressure (trace of the stress tensor) and internal energy of the solid phase, respectively. $Y_{{\rm s}i}$ and $M_{{\rm s}i}$ stand for the mass fraction and molar mass of the i-th species, and $\dot{\omega}_{{\rm s}i}$ and $\dot{\omega}'_{{\rm s}i}$ are the rates of change of its molar concentration due to homogeneous and heterogeneous reactions, respectively. Also, $\boldsymbol{\tau}_{\rm s}$ stands for the deviatoric part of the stress tensor, while $\boldsymbol{J}_{{\rm s}i}$ and $\boldsymbol{q}_{\rm s}$ denote the diffusion flux of the i-th species and the conductive heat flux of the solid phase, respectively.

Upon summation of equation (9) over all solid species, it follows that

$$\sum_{i=1}^{n}\dot{\omega}_{{\rm s}i}M_{{\rm s}i} \;=\; 0\,, \qquad \nabla\cdot(\phi_{\rm s}\boldsymbol{J}_{{\rm s}i}) \;=\; 0\,, \tag{12}$$

and

$$\mathcal{M} \;=\; -\sum_{i=1}^{n} \dot{\omega}'_{\mathrm{s}i} M_{\mathrm{s}i}\,. \tag{13}$$

Next, the Gibbs relation is introduced for each phase,

$$T\mathrm{d}s \;=\; \mathrm{d}e - \frac{p}{\rho^2}\mathrm{d}\rho - \sum_{i=1}^{r} \mu_i \mathrm{d}Y_i\,, \tag{14}$$

$$T_{\mathrm{s}}\mathrm{d}s_{\mathrm{s}} \;=\; \mathrm{d}e_{\mathrm{s}} - \sum_{i=1}^{n} \mu_{\mathrm{s}i} \mathrm{d}Y_{\mathrm{s}i}\,, \tag{15}$$

with T and T_{s} being the temperatures of the fluid and solid phases, and s and s_{s} the corresponding specific entropies. Also, μ_i and $\mu_{\mathrm{s}i}$ denote the chemical potential of the i-th species of the fluid and solid phase, respectively.

With regard to the Gibbs relation (15), it is worth recalling that, according to constitutive assumption (iii), the solid-phase density ρ_{s} is assumed constant, which is reasonable for the modeling of TFP. Nonetheless, this assumption can be removed if necessary.

Now let F denote the number of homogeneous reactions occurring in the fluid phase. The degree of advancement of the j-th reaction of them is denoted by ξ_j. Accordingly, in equation (2), $\dot{\omega}_i$ is expressed as

$$\dot{\omega}_i \;=\; \sum_{j=1}^{F} \nu_{ij} \dot{\xi}_j\,, \qquad i \;=\; 1, \ldots r\,, \tag{16}$$

with ν_{ij} being the stoichiometric coefficient of the i-th fluid species in the j-th (fluid) homogeneous reaction. This expression involves all fluid species and, therefore, a coefficient ν_{ij} can be zero.

Similarly, let S denote the number of homogeneous reactions occurring in the solid phase. The degree of advancement of the j-th reaction is denoted by $\dot{\xi}_{\mathrm{s}j}$. Then, in equation (9), $\dot{\omega}_{\mathrm{s}i}$ is expressed as

$$\dot{\omega}_{\mathrm{s}i} \;=\; \sum_{j=1}^{S} \nu_{\mathrm{s}ij}\, \dot{\xi}_{\mathrm{s}j}\,, \qquad i \;=\; 1, \ldots n\,, \tag{17}$$

with $\nu_{\mathrm{s}ij}$ being the stoichiometric coefficient of the i-th solid species in the j-th (solid) homogeneous reaction. Again, a coefficient $\nu_{\mathrm{s}ij}$ can be zero.

Also, let K be the number of heterogeneous reactions. The degree of advancement of the j-th reaction of them is denoted by $\dot{\xi}'_j$. Then the rates of change of the molar concentrations of the i-th species in the heterogeneous reactions for each phase are expressed as

$$\dot{\omega}'_i \;=\; \sum_{j=1}^{K} \nu'_{ij} \dot{\xi}'_j \,, \qquad i \;=\; 1, \ldots r \,, \tag{18}$$

$$\dot{\omega}_{\mathrm{s}i}' \;=\; \sum_{j=1}^{K} \nu_{\mathrm{s}ij}' \, \dot{\xi}'_j \,, \qquad i \;=\; 1, \ldots n \,. \tag{19}$$

In these relations, ν'_{ij} is the stoichiometric coefficient of the i-th fluid species in the j-th heterogeneous reaction and $\nu_{\mathrm{s}ij}'$ is the stoichiometric coefficient of the i-th solid species in it. Evidently, ν'_{ij} and $\nu_{\mathrm{s}ij}'$ can be zero.

It is also useful to introduce the affinities of the fluid and solid homogeneous reactions, $\mathcal{A}_j$ and $\mathcal{A}_{\mathrm{s}j}$, respectively,

$$\mathcal{A}_j \;=\; -\sum_{i=1}^{r} M_i \nu_{ij} \mu_i \,, \qquad j \;=\; 1, \ldots F \,, \tag{20}$$

$$\mathcal{A}_{\mathrm{s}j} \;=\; -\sum_{i=1}^{n} M_{\mathrm{s}i} \nu_{\mathrm{s}ij} \mu_{\mathrm{s}i} \,, \quad j \;=\; 1, \ldots S \,. \tag{21}$$

We also introduce the affinities $\mathcal{A}'_j$ of the heterogeneous reactions as follows

$$\mathcal{A}'_j \;=\; -\sum_{i\,=\,1}^{r} M_i \nu'_{ij} \mu_i - \frac{T}{T_{\mathrm{s}}} \sum_{i=1}^{n} M_{\mathrm{s}i} \nu_{\mathrm{s}ij}' \mu_{\mathrm{s}i}, \qquad j \;=\; 1, \ldots K \,. \tag{22}$$

By substituting the balance equations of each phase into the corresponding Gibbs relation, (14) or (15), the rates of change of the specific entropies

can be written as

$$\phi\rho T\frac{\mathrm{d}s}{\mathrm{d}t} \;=\; \phi\boldsymbol{\sigma}^{\mathrm{v}} : \boldsymbol{V} - \nabla\cdot(\phi\boldsymbol{q}) + \mathcal{E} - \sum_{i=1}^{r}\mu_i\left(\dot{\omega}_i M_i + \dot{\omega}_i' M_i - \nabla\cdot(\phi\boldsymbol{J}_i)\right)$$
$$- (\boldsymbol{f} - p\nabla\phi)\cdot\boldsymbol{u} - \mathcal{M}\left(h - \frac{1}{2}\boldsymbol{u}\cdot\boldsymbol{u} - \frac{p}{\rho_{\mathrm{s}}} - \sum_{i=1}^{r}\mu_i Y_i\right), \qquad (23)$$

$$\phi_{\mathrm{s}}\rho_{\mathrm{s}}T_{\mathrm{s}}\frac{\mathrm{d}s_{\mathrm{s}}}{\mathrm{d}t} \;=\; -\nabla\cdot(\phi_{\mathrm{s}}\boldsymbol{q}_{\mathrm{s}}) - \mathcal{E} - \sum_{i=1}^{n}\mu_{\mathrm{s}i}\left(\dot{\omega}_{\mathrm{s}i}M_{\mathrm{s}i} + \dot{\omega}_{\mathrm{s}i}' M_{\mathrm{s}i} - \nabla\cdot(\phi_{\mathrm{s}}\boldsymbol{J}_{\mathrm{s}i})\right)$$
$$+ \mathcal{M}\left(e_{\mathrm{s}} - \sum_{i=1}^{n}\mu_{\mathrm{s}i}Y_{\mathrm{s}i}\right). \qquad (24)$$

In these equations, $h = e + \frac{p}{\rho}$ is the specific enthalpy of the fluid phase, and $\boldsymbol{V}$ is the deformation-rate tensor.

The next step is to derive the balance law for the mixture's entropy. To this end, the mixture's density ρ_{m}, barycentric velocity $\boldsymbol{u}_{\mathrm{m}}$, and specific entropy s_{m} are introduced,

$$\rho_{\mathrm{m}} \;=\; \phi\rho + \phi_{\mathrm{s}}\rho_{\mathrm{s}}, \qquad \boldsymbol{u}_{\mathrm{m}} \;=\; \frac{\phi\rho\boldsymbol{u}}{\rho_{\mathrm{m}}}, \qquad s_{\mathrm{m}} \;=\; \frac{\phi\rho s + \phi_{\mathrm{s}}\rho_{\mathrm{s}}s_{\mathrm{s}}}{\rho_{\mathrm{m}}}. \qquad (25)$$

Also, let $\mathrm{d}/\mathrm{d}_{\mathrm{m}}t\,()$ denote the material derivative with respect to the mixture's barycentric velocity, $\mathrm{d}/\mathrm{d}_{\mathrm{m}}t() \;=\; (\partial/\partial t + \boldsymbol{u}_{\mathrm{m}}\cdot\nabla)()$. By taking the material derivative of s_{m} and by substituting (23) and (24), we arrive at an equation of the form

$$\rho_{\mathrm{m}}\frac{\mathrm{d}s_{\mathrm{m}}}{\mathrm{d}_{\mathrm{m}}t} \;=\; \nabla\cdot\boldsymbol{J} + \sigma\,, \qquad (26)$$

where $\boldsymbol{J}$ and σ denote the mixture's entropy flux and production rate, respectively. The latter obeys the entropy inequality

$$\sigma \;\geq\; 0\,. \qquad (27)$$

More specifically, the expression for $\boldsymbol{J}$ reads

$$\boldsymbol{J} \;=\; -\frac{\phi}{T}\boldsymbol{q} - \frac{\phi_{\mathrm{s}}}{T_{\mathrm{s}}}\boldsymbol{q}_{\mathrm{s}} + \phi\rho s\left(\boldsymbol{u}_{\mathrm{m}} - \boldsymbol{u}\right) + \phi_{\mathrm{s}}\rho_{\mathrm{s}}s_{\mathrm{s}}\boldsymbol{u}_{\mathrm{m}}$$
$$+ \frac{\phi}{T}\sum_{i=1}^{r}\mu_i\boldsymbol{J}_i + \frac{\phi_{\mathrm{s}}}{T_{\mathrm{s}}}\sum_{i=1}^{n}\mu_{\mathrm{s}i}\boldsymbol{J}_{\mathrm{s}i}\,, \qquad (28)$$

while that of σ reads

$$\begin{aligned}\sigma \;=\; & \frac{\phi}{T}\boldsymbol{\sigma}^{\mathrm{v}} : \boldsymbol{V} + \phi\boldsymbol{q}\cdot\nabla\left(\frac{1}{T}\right) + \phi_{\mathrm{s}}\boldsymbol{q}_{\mathrm{s}}\cdot\nabla\left(\frac{1}{T_{\mathrm{s}}}\right) + \mathcal{E}\left(\frac{1}{T}-\frac{1}{T_{\mathrm{s}}}\right) \\ & - (\boldsymbol{f} - p\nabla\phi)\cdot\frac{1}{T}\boldsymbol{u} - \sum_{i=1}^{r}\phi\boldsymbol{J}_i\cdot\nabla\left(\frac{\mu_i}{T}\right) - \sum_{i=1}^{n}\phi_{\mathrm{s}}\boldsymbol{J}_{\mathrm{s}i}\cdot\nabla\left(\frac{\mu_{\mathrm{s}i}}{T_{\mathrm{s}}}\right) \\ & + \frac{1}{T}\sum_{j=1}^{F}\mathcal{A}_j\dot{\xi}_j + \frac{1}{T_{\mathrm{s}}}\sum_{j=1}^{S}\mathcal{A}_{\mathrm{s}j}\dot{\xi}_{\mathrm{s}j} + \frac{1}{T}\sum_{j=1}^{K}\mathcal{A}'_j\dot{\xi}'_j - \mathcal{M}\hat{\mathcal{A}}\,, \end{aligned} \tag{29}$$

where $\hat{\mathcal{A}}$ is given by

$$\hat{\mathcal{A}} \;=\; \frac{p}{\rho_{\mathrm{s}}}\left(\frac{1}{T_{\mathrm{s}}}-\frac{1}{T}\right) - \frac{1}{2T}\boldsymbol{u}\cdot\boldsymbol{u}\,. \tag{30}$$

Each term in the entropy production rate is associated with a specific irreversible process. Moreover, each term can be expressed as the product between a yet-to-be-determined quantity, referred to as thermodynamic current, and another term referred to as thermodynamic force.

2.2. Constitutive relations

The system of governing equations (1)–(4) and (8)–(11) is closed by appropriate constitutive relations for the thermodynamic currents in terms of the thermodynamic forces. With the exception of the reaction rates, which are discussed in the next subsection, the constitutive relations between currents and forces are assumed to be linear. This is essentially an application of the classical theory of irreversible processes [27, 28] to two-phase systems.

Regarding the viscous stress tensor $\boldsymbol{\sigma}^{\mathrm{v}}$, it is noted that it is symmetric by virtue of the conservation of angular momentum. Further, it is decomposed as follows

$$\boldsymbol{\sigma}^{\mathrm{v}} \;=\; -p^{\mathrm{v}}\boldsymbol{I} + \boldsymbol{\sigma}^{\mathrm{v}}_d\,, \tag{31}$$

where p^{v} is the bulk viscous pressure and $\boldsymbol{\sigma}^{\mathrm{v}}_d$ is the deviatoric component of $\boldsymbol{\sigma}^{\mathrm{v}}$. According to assumption (iii), the fluid is isotropic and Newtonian, the corresponding constitutive relations read

$$\boldsymbol{\sigma}^{\mathrm{v}}_d \;=\; 2\eta\boldsymbol{V}^{\mathrm{d}}\,, \qquad p^{\mathrm{v}} \;=\; -\zeta\nabla\cdot\boldsymbol{u}\,, \tag{32}$$

where $\boldsymbol{V}^{\mathrm{d}}$ is the deviatoric component of the deformation-rate tensor, and η and ζ are the shear and bulk viscosities, respectively, of the fluid.

In TFP, it is reasonable to assume Newtonian behavior in the early stages of polymerization because the liquid mixture exhibits relatively low viscosity and the chain growth is limited. But as conversion progresses, viscosity increases and viscoelastic effects may develop due to the forming polymer network. This implies that in single-phase modeling of TFP, non-Newtonian constitutive relations are preferable in order to account for the presence of polymer molecules inside the reaction zones. However, in the proposed two-phase framework, this is no longer the case because the polymer is treated as a distinct solid material.

With regard to heat diffusion, its flux is composed of two contributions: the first one is due to heat conduction and described by Fourier's law, and the second one is due to molecular diffusion between species with different enthalpies. In this study, for the purposes of simplicity, the second contribution is assumed to be negligible; nonetheless, it can be readily taken into account if it is deemed appropriate. Therefore, the conductive heat fluxes for the two phases are expressed as

$$\boldsymbol{q} \;=\; -\kappa \nabla T\,, \quad \text{and} \quad \boldsymbol{q}_{\mathrm{s}} \;=\; -\kappa_{\mathrm{s}} \nabla T_{\mathrm{s}}\,, \tag{33}$$

where κ and κ_{s} are the thermal conductivities of the two phases. In general, the solid phase is anisotropic, in which case κ_{s} is a second-order tensor. In the context of TFP, the solid phase is typically assumed to be isotropic and, therefore, κ_{s} reduces to a scalar.

Similarly, the diffusion fluxes of the fluid and solid species are given by Fick's law,

$$\boldsymbol{J}_i \;=\; -\,\rho \mathcal{D}_i \nabla Y_i\,, \qquad i = 1, \dots r\,, \tag{34}$$

$$\boldsymbol{J}_{\mathrm{s}i} \;=\; -\,\rho_{\mathrm{s}} \mathcal{D}_{\mathrm{s}i} \nabla Y_{\mathrm{s}i}\,, \qquad i = 1, \dots n\,, \tag{35}$$

where $\mathcal{D}_i$ and $\mathcal{D}_{\mathrm{s}i}$ are the mass diffusivity of the i-th fluid and solid species, respectively.

In the linear regime, the constitutive relation for the interfacial momentum exchange $\boldsymbol{f}$ reads

$$\boldsymbol{f} \;=\; p \nabla \phi - \delta \boldsymbol{u}\,. \tag{36}$$

The second term in the previous relation represents the interfacial drag, with δ denoting the corresponding drag coefficient. Its value depends on the liquid viscosity and the microstructure of the solid polymer.

Finally, the interfacial heat exchange is given by the following constitutive relation

$$\mathcal{E} \;=\; \lambda(T - T_{\rm s})\,, \tag{37}$$

where λ is the interfacial heat-exchange coefficient. Its value depends on the thermal conductivities of the materials in the two phases and the microstructure of the solid polymer.

With regard to TFP, the velocities of the liquid substances are very small; in fact, they are orders of magnitude smaller than the speed of sound. Accordingly, one can simplify the governing system by perturbing it at the zero-Mach number limit. According to this approach, the Mach number is introduced as a perturbation parameter and all variables are expanded into an asymptotic power series in terms of this parameter [26, 29]. The low-Mach number approximation of the governing system for the fluid phase reads

$$\frac{\partial \phi\rho}{\partial t} + \nabla\cdot(\phi\rho\boldsymbol{u}) \;=\; \mathcal{M}\,, \tag{38}$$

$$\begin{aligned}\phi\rho\frac{{\rm d}Y_i}{{\rm d}t} \;&=\; \dot\omega_i M_i + \dot\omega_i' M_i \\ &\quad - \mathcal{M}Y_i - \nabla\cdot(\phi\boldsymbol{J}_i)\,, \qquad i \;=\; 1,\ldots r-1\,,\end{aligned} \tag{39}$$

$$\phi\rho\frac{{\rm d}\boldsymbol{u}}{{\rm d}t} + \phi\nabla p \;=\; \nabla\cdot(\phi\boldsymbol{\sigma}^{\rm v}) - \phi\rho\boldsymbol{g} - \delta\boldsymbol{u} - \mathcal{M}\boldsymbol{u}\,, \tag{40}$$

$$\begin{aligned}\phi\rho\frac{{\rm d}h^{\rm s}}{{\rm d}t} \;&=\; \phi\frac{{\rm d}p^0}{{\rm d}t} - \sum_{i=1}^{r} h_i^{\rm f}\left(\dot\omega_i M_i + \dot\omega_i' M_i - \nabla\cdot(\phi\boldsymbol{J}_i)\right) \\ &\quad - \nabla\cdot(\phi\boldsymbol{q}) + \mathcal{E} - \mathcal{M}\left(h^{\rm s} - \frac{p^0}{\rho_{\rm s}}\right)\,.\end{aligned} \tag{41}$$

In deriving this system, the fluid enthalpy is decomposed as the sum of sensible and formation enthalpies,

$$h = h^{\rm s} + \sum_{i=1}^{r} h_i^{\rm f} Y_i \tag{42}$$

with $h_i^{\rm f}$ being the formation enthalpy of the i-th fluid species. For the problems of interest and the liquids involved, the sensible enthalpy depends only on temperature, i.e. ${\rm d}h^{\rm s} = c_p{\rm d}T$ with c_p being the specific heat capacity of the fluid mixture. Also, p^0 is the first-order term of the expansion of

the pressure and is referred to as the thermodynamic pressure, whereas the second-order term is the dynamic pressure and is denoted by p. According to the low-Mach number expansion, p^0 is a function of time only.

Further, the governing system of balance laws for the solid phase can be expressed as

$$\rho_{\mathrm{s}}\frac{\partial \phi_{\mathrm{s}}}{\partial t} = -\mathcal{M}\,, \tag{43}$$

$$\phi_{\mathrm{s}}\rho_{\mathrm{s}}\frac{\partial Y_{\mathrm{s}i}}{\partial t} = \left(\dot{\omega}_{\mathrm{s}i} + \dot{\omega}_{\mathrm{s}i}'\right) M_{\mathrm{s}i} + \mathcal{M}Y_{\mathrm{s}i} - \nabla\cdot\left(\phi_{\mathrm{s}}\boldsymbol{J}_{\mathrm{s}i}\right)\,, \quad i = 1,\ldots n-1\,, \tag{44}$$

$$p_{\mathrm{s}}^0 = p^0\,, \tag{45}$$

$$\phi_{\mathrm{s}}\rho_{\mathrm{s}}\frac{\partial h_{\mathrm{s}}^{\mathrm{s}}}{\partial t} = \phi_{\mathrm{s}}\frac{\mathrm{d}p^0}{\mathrm{d}t} - \nabla\cdot\left(\phi_{\mathrm{s}}\boldsymbol{q}_{\mathrm{s}}\right) - \mathcal{E} + \mathcal{M}h_{\mathrm{s}}^{\mathrm{s}}\,, \tag{46}$$

where the sensible enthalpy of the solid phase, $h_{\mathrm{s}}^{\mathrm{s}}$, satisfies $\mathrm{d}h_{\mathrm{s}}^{\mathrm{s}} = c_{\mathrm{s}}\mathrm{d}T_{\mathrm{s}}$, with c_{s} being the specific heat capacity of the solid. Also, as a result of assumption (iii), the momentum equation for the solid phase (10) is inconsequential. This is deemed sufficient for the purposes of modeling TFP. Nonetheless, assumption (iii) can be removed, in which case the momentum equation for the solid phase must also be solved. This can be relevant, for example, when thermal stresses are significant.

2.3. Coupling with a chemical kinetics mechanism for TFP

The governing system (38)–(41) and (43)–(46) is quite general and can be coupled with any suitable chemical kinetics mechanism. Herein we consider a reduced mechanism for TFP that has been used extensively in the literature. It is a three-step chain mechanism [11] that consists of initiation (decomposition), propagation, and termination steps. Generally, in the initiation step, when applying heat, the initiator decomposes into primary free radicals. These primary radicals subsequently react with monomer molecules to form polymer radicals. During the propagation step, these polymer radicals continue to react, extending the polymer chain and producing heavier radicals. In the termination step, the active radicals combine, resulting in the formation of a non-reacting polymer product. The kinetics mechanism

reads,

$$\mathrm{I}_{(l)} \xrightarrow{k_\mathrm{d}} 2f\,\mathrm{R}_{(s)}, \tag{47}$$

$$\mathrm{R}_{(s)} + \mathrm{M}_{(l)} \xrightarrow{k_\mathrm{p}} \mathrm{R}_{(s)} + \mathrm{Heat}\,, \tag{48}$$

$$\mathrm{R}_{(s)} + \mathrm{R}_{(s)} \xrightarrow{k_\mathrm{t}} \mathrm{P}_{(s)}\,. \tag{49}$$

In these reactions, $\mathrm{I}, \mathrm{R}, \mathrm{M}$ and P denote the initiator, radical, monomer and polymer, respectively, while k_d, k_p, and k_t denote the rate coefficients of decomposition, propagation, and termination, respectively.

Further, f is the decomposition efficiency. For modeling purposes, primary and polymer radicals are assumed to share the same reaction rate. The initiator and monomer are liquid, while the radical and polymer product are assumed to be solid. In this context, it is important to note that, in TFP, the propagation reaction is exothermic while the other ones are essentially neutral. In other words, the heat that sustains the front is released in the propagation reaction. This contrasts with combustion processes, where heat is released in the termination steps.

In TFP, initiators generally have higher enthalpies of formation than monomers due to the presence of weak chemical bonds. However, their concentration in the liquid mixture is typically very low; for example, it is 1% in [30] and 0.3% in [11]. Therefore, the contribution of the initiator's enthalpy of formation can be neglected, and only the monomer's formation enthalpy h^f_M is considered in the present model. Thus, the enthalpy of reaction, Δh_poly, is approximated as $\Delta h_\mathrm{poly} = h^\mathrm{f}_\mathrm{s} - h^\mathrm{f}_\mathrm{M} < 0$. It is noted that the formation enthalpy of the solid polymer h^f_s is typically much lower than that of the liquid monomer solution. This reflects the greater thermodynamic stability of the polymer due to stronger bonds compared to those of the less stable monomer solution.

Based on the kinetics model described in (47)–(49), the rates of change of the concentrations of the individual species follow directly from the mass action law,

$$\dot{\omega}'_\mathrm{I} = -k_\mathrm{d}\, c_\mathrm{I}\, \phi\,, \tag{50}$$

$$\dot{\omega}'_\mathrm{M} = -k_\mathrm{p}\, c_\mathrm{R}\, c_\mathrm{M}\, \phi\, \phi_\mathrm{s}\,, \tag{51}$$

$$\dot{\omega}'_\mathrm{R} = 2f\, k_\mathrm{d}\, c_\mathrm{I}\, \phi\,, \tag{52}$$

$$\dot{\omega}_\mathrm{R} = -2k_\mathrm{t}\, (c_\mathrm{R}\phi_\mathrm{s})^2\,, \tag{53}$$

$$\dot{\omega}_\mathrm{P} = k_\mathrm{t}\, (c_\mathrm{R}\, \phi_\mathrm{s})^2\,, \tag{54}$$

where $c_{\rm I}$, $c_{\rm M}$, $c_{\rm R}$, and $c_{\rm P}$ denote the corresponding molar concentrations of initiator, monomer, radical, and polymer, respectively. Therefore, $c_{\rm I} = \rho Y_{\rm I}/M_{\rm I}$ and so on and so forth. It is worth observing that, according to these rates, the concentration of each species is scaled by the volume fraction of its corresponding phase.

The previous system can be simplified by invoking the steady-state approximation for the radical R, which is highly reactive. According to it,

$$\dot{\omega}_{\rm R} + \dot{\omega}'_{\rm R} \;=\; 2f\, k_{\rm d}\, c_{\rm I}\, \phi - 2k_{\rm t}\, \left(c_{\rm R}\, \phi_{\rm s}\right)^2 \simeq 0\,, \tag{55}$$

from which we readily get

$$c_{\rm R}\, \phi_{\rm s} \;=\; \sqrt{f\, \frac{k_{\rm d}}{k_{\rm t}}\, c_{\rm I}\, \phi}\,. \tag{56}$$

The rate coefficients $k_{\rm d}$, $k_{\rm p}$ and $k_{\rm t}$ are given by Arrhenius laws,

$$k_{\rm d} \;=\; k^0_{\rm d}\, {\rm e}^{-E_{\rm d}/RT}\,, \qquad k_{\rm p} \;=\; k^0_{\rm p}\, {\rm e}^{-E_{\rm p}/RT}\,, \qquad k_{\rm t} \;=\; k^0_{\rm t}\, {\rm e}^{-E_{\rm t}/RT}\,, \tag{57}$$

with $k^0_{\rm d}$, $k^0_{\rm p}$, and $k^0_{\rm t}$ the pre-exponential factors and $E_{\rm d}$, $E_{\rm p}$, and $E_{\rm t}$ the activation energies for the decomposition, propagation, and termination reactions, respectively. It is noted that the constitutive relations for the reaction rates are nonlinear, in contrast to those for the other thermodynamic currents that enter equation (29). Further, in relation to frontal polymerization, the kinetic energy of the liquid in the reaction zone is much smaller than the heat release, which implies that the last term in (29) is also much smaller than the terms involving the reaction rates, thereby ensuring the positivity of σ under the presumed Arrhenius kinetics laws. In other words, since the kinetic energy is relatively small, there is no need to modify the Arrhenius kinetics laws in order to deal with the last term on the right-hand side of (29).

3. Final form of the two-phase model

The expressions for the species concentration rates can readily be substituted in the governing system of equations (38)–(41) and (43)–(46). Also, in TFP, mass diffusion is typically neglected. In such systems, thermal diffusion of the liquid species is at least two orders of magnitude faster than mass diffusion, as mentioned in [11]. Further, mass diffusion in solids is much

weaker than in liquids. For this reason, in the present study, mass diffusion has been neglected in both phases.

Additionally, in TFP studies, bulk viscous stresses are typically negligible. This assumption is also followed herein. Also, we assume that the two phases are in thermal equilibrium, i.e. $T_\mathrm{s} = T$, and that the heat capacities of both phases are constant. These approximations are introduced for the purpose of simplifying the governing equations and are deemed reasonable in TFP. Nonetheless, they can be removed if necessary. Since the temperatures of both phases are considered equal, one can add the energy equations (41) and (46) to obtain a single energy equation for the entire two-phase system. Further, in TFP, the domain is open and, therefore, the thermodynamic pressure p^0 is constant and equal to the ambient pressure.

With these assumptions, and with the chemical-kinetics mechanism elaborated earlier, the final form of the two-phase model for TFP reads,

$$\frac{\partial \phi\rho}{\partial t} + \nabla\cdot(\phi\rho\boldsymbol{u}) = \mathcal{M}\,, \tag{58}$$

$$\phi\rho\frac{\mathrm{d}Y_\mathrm{I}}{\mathrm{d}t} = \dot{\omega}'_\mathrm{I}M_\mathrm{I} - \mathcal{M}Y_\mathrm{I}\,, \tag{59}$$

$$\phi\rho\frac{\mathrm{d}\boldsymbol{u}}{\mathrm{d}t} + \phi\nabla p = \nabla\cdot\left(2\phi\eta\boldsymbol{V}^\mathrm{d}\right) - \phi\rho\boldsymbol{g} - \delta\boldsymbol{u} - \mathcal{M}\boldsymbol{u}\,, \tag{60}$$

$$\rho_\mathrm{s}\frac{\partial\phi_\mathrm{s}}{\partial t} = -\mathcal{M}\,, \tag{61}$$

$$\begin{aligned}\left(\phi\rho c_p + \phi_\mathrm{s}\rho_\mathrm{s}c_\mathrm{s}\right)\frac{\partial T}{\partial t} &= -\phi\rho c_p\boldsymbol{u}\cdot\nabla T + \nabla\cdot\left(\left(\phi\kappa + \phi_\mathrm{s}\kappa_\mathrm{s}\right)\nabla T\right) - h^\mathrm{f}_\mathrm{M}\dot{\omega}'_\mathrm{M}M_\mathrm{M}\\ &\quad - \mathcal{M}\left(\left(c_p - c_\mathrm{s}\right)\left(T - T_\mathrm{ref}\right) - \frac{p^0}{\rho_\mathrm{s}}\right)\,,\end{aligned} \tag{62}$$

with $\phi + \phi_\mathrm{s} = 1$, $Y_\mathrm{I} + Y_\mathrm{M} = 1$, and T_ref a reference temperature. Also, in the above system,

$$\mathcal{M} \;=\; \dot{\omega}'_\mathrm{I}M_\mathrm{I} + \dot{\omega}'_\mathrm{M}M_\mathrm{M}\,, \tag{63}$$

with

$$\dot{\omega}'_\mathrm{I} \;=\; -\frac{1}{M_\mathrm{I}}k_\mathrm{d}\phi\rho Y_\mathrm{I}\,, \tag{64}$$

and

$$\dot{\omega}'_\mathrm{M} \;=\; -\frac{1}{M_\mathrm{M}}k_p\phi\rho Y_\mathrm{M}\sqrt{\frac{f}{M_\mathrm{I}}\frac{k_\mathrm{d}}{k_\mathrm{t}}\phi\rho Y_\mathrm{I}}\,. \tag{65}$$

It is worth noting that, in polymerization systems, the growth of polymer chains proceeds continuously as the reaction advances. Consequently, both radical species and polymer product attain progressively larger chain lengths, leading to substantial increases in their molar masses within the solid phase. Reported values can reach the order of 10^3 kg/mol [7], compared to the molar mass of typical initiators and monomers, which are on the order of 10^{-1} kg/mol. This behavior is fundamentally opposite to that in combustion processes, where larger fuels are decomposed into smaller, gaseous molecules. Since the molar masses of the radical and polymer, M_{R} and M_{P}, cannot be explicitly determined within the context of the employed chemical kinetics mechanism, the governing system (58)–(62) does not include separate balance laws for the mass fractions of the solid species. Nonetheless, more detailed modeling can incorporate the evolution and growth of these molar masses to capture the full composition of the solid phase.

Also, regarding the drag coefficient δ, the solid phase can be approximated as an assembly of parallel and randomly distributed cylinders of equal diameter d_{p}. Then, by considering the average drag acting on a single cylindrical element and by multiplying it with the number density of cylinders [31], one gets

$$\delta \;=\; \frac{128\mu}{\pi d_{\mathrm{p}}^2}\,\phi_{\mathrm{s}}\,. \tag{66}$$

It is noted that this relation is introduced as a simple approximation to take into account the effect of interfacial drag in polymerization, while ensuring compliance with the entropy inequality. In addition, to the best of our knowledge, there is currently a lack of experimental data or empirical correlations for the interfacial drag coefficient δ in the problem in hand. Nonetheless, more detailed descriptions that are consistent with a given polymer microstructure can also be developed. One option is to derive a correlation for the interfacial drag coefficient from existing single-phase (mixture) models of TFP. In such models the effects of the interfacial drag is taken into account implicitly by assuming a dependence of the mixture viscosity η on the volume fraction of the solid. One can then try to derive correlations for the drag coefficient by mapping it to existing models for the mixture viscosity.

The numerical method that is used to solve the system (58)–(62) is a generalization of the time-accurate algorithm [32] for single-phase low-Mach number flows. This is a finite-volume method with second-order accuracy in both space and time. According to it, spatial gradients are approximated via

centered differences. Time integration is performed via a two-stage predictor–corrector scheme. This approach is adopted to enhance temporal accuracy while ensuring numerical stability. In each stage, the various terms are integrated explicitly via an Adams–Bashforth scheme, with the exception of the drag term and the viscous flux in the direction of the gravitational acceleration in the momentum equation. These terms are integrated via the semi-implicit Crank–Nicolson scheme. Consistent coupling between the dynamic pressure and velocity field is achieved in the projection steps, which amount to combining the divergence of the momentum equation with the continuity equation. This results in a linear elliptic equation that is discretized and solved numerically.

This algorithm has been implemented in a collocated grid arrangement and employs a flux-interpolation technique to remedy the odd-even decoupling problem associated with such grids. It has been validated for single-phase flows in [32] and employed in the study of low-Mach number flows in mixed porous–pure fluid domains in [26, 33–35] and elsewhere. The complete algorithm is provided in Appendix Appendix A. For our simulations of TFP, this algorithm has been parallelized using the Message Passing Interface (MPI) protocol.

4. Validation tests

In this section, we present results from validation tests that we conducted in the context of our study. Since existing TFP models are based on the single-phase approach and most of them do not involve a momentum equation, we first present a reduced, reaction-diffusion version of the full TFP model (58)–(62). Henceforth, this reduced version will be referred to as the *reduced RD model*.

The reduced RD model is derived by setting the fluid velocity equal to zero. However, with zero velocity, the continuity equations (58) and (61) cannot be satisfied simultaneously unless $\rho = \rho_\mathrm{s}$. Therefore, to satisfy mass conservation, the liquid and solid densities have to be equal and constant. Under these assumptions, the reduced RD model reads,

$$\rho \;=\; \rho_\mathrm{s} \;=\; \text{const.} \tag{67}$$

From the earlier assumptions, equations (58)–(62) reduce to

$$\rho \frac{\partial \phi}{\partial t} = \mathcal{M}\,, \tag{68}$$

$$\phi\rho \frac{\partial Y_{\rm I}}{\partial t} = \dot{\omega}'_{\rm I} M_{\rm I} - \mathcal{M} Y_{\rm I}\,, \tag{69}$$

$$\nabla p = 0\,, \tag{70}$$

$$\rho_{\rm s} \frac{\partial \phi_{\rm s}}{\partial t} = -\mathcal{M}\,, \tag{71}$$

$$\begin{aligned}(\phi\rho c_p + \phi_{\rm s}\rho_{\rm s} c_{\rm s}) \frac{\partial T}{\partial t} &= -\nabla\cdot(\phi \boldsymbol{q} + \phi_{\rm s}\boldsymbol{q}_{\rm s}) - h^{\rm f}_{\rm M}\dot{\omega}'_{\rm M} M_{\rm M} \\ &\quad - \mathcal{M}\left((c_p - c_{\rm s})(T - T_{\rm ref}) - \frac{p^0}{\rho_{\rm s}}\right)\,. \end{aligned} \tag{72}$$

It is noted that even though the momentum equation becomes inconsequential, the reduced RD model still involves two phases. In the validation tests presented below, this model is treated numerically with the same algorithm that is developed for the full model, in which we set $\boldsymbol{u} = 0$.

The case that we consider for validation purposes corresponds to a stable polymerization front. Accordingly, the propagation speed is constant and so are the profiles of the variables inside the reaction zone. This case was studied numerically by Tiani in [30] who used a single-phase reaction-diffusion model and the three-step chemical kinetics scheme described earlier. Henceforth, it will be referred to as *case 1*.

The setup of this case is as follows. We consider a 1D domain of length L. Initially, the domain is filled with a liquid mixture of monomer and initiator ($\phi = 1$) at uniform temperature T_0. The initiator concentration is $Y_{\rm I} = 0.003$. The left boundary, located at $x = 0$, is a rigid wall at higher (ignition) temperature $T_{\rm i} > T_0$. Due to the higher temperature, a polymerization front is established that propagates to the right at constant speed $V_{\rm f}$. The values of the various parameters and constants for this case are provided in Table 1 below. It is noted that the value of the monomer's formation enthalpy $h^{\rm f}_{\rm M}$ is the one at the initial temperature T_0.

At the left wall, the zero-Neumann condition is prescribed for all other variables besides the temperature. At the right boundary, $x = L$, zero-Neumann conditions are prescribed for all variables. In summary, the bound-

ary conditions are

$$x = 0: \quad \frac{\partial \phi}{\partial x} = \frac{\partial p}{\partial x} = \frac{\partial Y_{\mathrm{I}}}{\partial x} = 0, \quad T = T_{\mathrm{i}}, \tag{73}$$

$$x = L: \quad \frac{\partial \phi}{\partial x} = \frac{\partial p}{\partial x} = \frac{\partial Y_{\mathrm{I}}}{\partial x} = \frac{\partial T}{\partial x} = 0. \tag{74}$$

Variable	Value	Variable	Value
ρ	800 kg/m^3	k^0_{eff}	1.03×10^8 m$^{3/2}$/(s mol$^{1/2}$)
f	0.5	k^0_{d}	4×10^{12} 1/s
T_0	340 K	k^0_{p}	1.26×10^4 m^3/(s mol)
T_{a}	920 K	k^0_{t}	3×10^4 m^3/(s mol)
T_{i}	920 K	E_{d}	1.7×10^5 J/mol
l_{ref}	1.4×10^{-6} m	E_{p}	1×10^4 J/mol
t_{ref}	9.46×10^{-6} s	E_{t}	2×10^4 J/mol
η_{ref}	1.5×10^{-4} Pa s	E_{eff}	8.5×10^4 J/mol
c_p	600 J/(kg K)	$c_{\mathrm{I}}(0)$	10 mol/m^3
c_{s}	540 J/(kg K)	$c_{\mathrm{M}}(0)$	1000 mol/m^3
κ	0.1 W/(m K)	M_{I}	0.242 kg/mol
κ_{s}	0.086 W/(m K)	M_{M}	0.798 kg/mol
α	3×10^{-4} 1/K	$h^{\mathrm{f}}_{\mathrm{M}}$	7.95×10^5 J/mol

Table 1: Case 1: values of the various parameters and constants.

Tiani [30] presented results for the dimensionless temperature and initiator concentration, θ and J respectively, which are defined as follows,

$$\theta = \frac{T - T_{\mathrm{a}}}{\beta_{\mathrm{s}} T_{\mathrm{a}}}, \qquad J = \sqrt{\frac{\phi c_{\mathrm{I}}}{c_{\mathrm{I}}(0)}}. \tag{75}$$

$T_{\mathrm{a}}, \beta_{\mathrm{s}}$ and $c_{\mathrm{I}}(0)$ are a constant temperature, dimensionless inverse of the effective activation energy, and the initial concentration of the initiator, respectively.

Behind the reaction front, θ attains a positive peak. In contrast, in the unreacted monomer region ahead of the front, T remains close to T_{ref} and therefore below T_{a}, resulting in negative values of θ. For the initiator, $J = 1$ in the unreacted region ahead of the front, whereas in the reacted region behind the front the initiator has been consumed, yielding $J < 1$. Consequently, J ranges between 0 and 1. The reference temperature is T_0. As for

the reference length and time, they are defined as

$$t_{\rm ref} \;=\; \frac{\exp\left(1/\beta_{\rm s}\right)}{k^0_{\rm eff}\sqrt{c_{\rm I}\left(0\right)}}\,, \qquad l_{\rm ref} \;=\; \sqrt{\frac{\kappa\, t_{\rm ref}}{\rho_{\rm ref}\, c_p}}\,, \tag{76}$$

where $k^0_{\rm eff} = k^0_{\rm p}\sqrt{f k^0_{\rm d}/k^0_{\rm t}}$ is the effective reaction rate pre-exponential factor. Below, we provide results for θ, J, and the front speed $V_{\rm f}$ (nondimensionalized by $l_{\rm ref}/t_{\rm ref}$). Also, in the presentation of the results, distance x and time t are nondimensionalized by $l_{\rm ref}$ and $t_{\rm ref}$, respectively.

First, we present results of a numerical convergence study using the reduced RD model. The computational domain has a length $L = 60$ and is discretized into n uniform computational segments. We consider four different grids, R_1, R_2, R_3, and R_4 that consist of $n = 500$, 1000, 2000, and 4000 cells, respectively. Numerical convergence is assessed by computing the relative error in the computation of the front speed, $V_{\rm f}$, and the integral of the temperature over the entire domain, I, The dimensionless temperature integral I is defined as

$$I \;=\; \int_0^L \theta(x,t)dx\,. \tag{77}$$

In other words, I is a measure of the sensible enthalpy of the system.

The relative error is the normalized difference between the numerical prediction with a given grid and that with the finest grid R_4. Accordingly, the relative error in the computation of I is $E_I(R_i) = (I(R_i) - I(R_4))/I(R_4)$ for $i = 1$, 2, 3 and similarly for the relative error in the front speed. The values of these errors at time $t = 40$ are shown in Figure 1. According to Figure 1, the relative error for both quantities drops very fast with grid refinement, which is an indication of the good accuracy of the proposed algorithm. In fact, the predictions for I and $V_{\rm f}$ with the grid R_3 are practically identical to those with R_4.

We proceed to compare our numerical results, obtained with the RD model, with those of [30]. Figure 2 shows the evolution of front speed with time. The location of the reaction front is assumed to be the location of maximum monomer consumption rate $\dot{\omega}_{\rm M}$. The front speed $V_{\rm f}$ is then computed on the basis of this assumption. Both simulations predict an initial overshoot of the velocity during the transient phase, before the establishment of a front with constant propagation speed. This overshoot is likely due to the influence of the heated wall. Further, the predictions for the steady-state

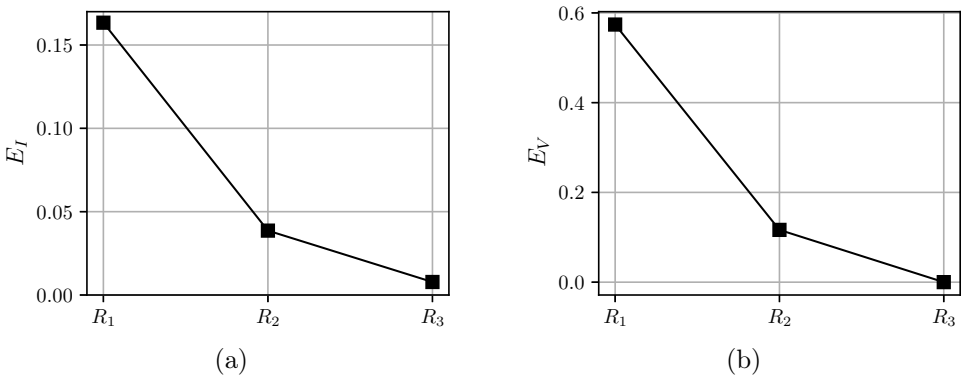


Figure 1: Numerical convergence study of case 1: relative error of (a) the temperature integral I and (b) the front speed V_f with different grid resolutions.

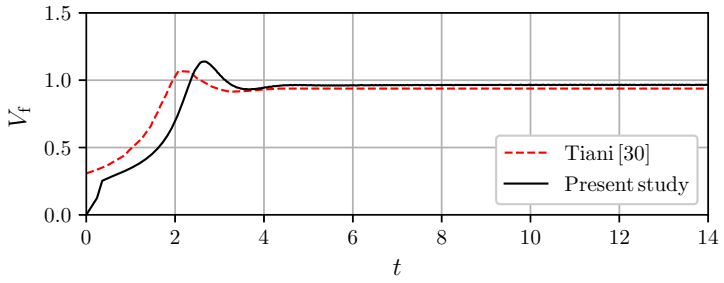


Figure 2: Case 1: evolution of the front speed V_f with time. In the early stages, there is an overshoot in V_f due to presence of the heated wall, before the establishment of a steady front. The solid line corresponds to the profile obtained with the reduced RD model of the present study.

value of V_f are very close, as is the time at which this value is attained (at approximately $t \approx 4$). The value of V_f predicted in the present study is 2.96% lower than that in [30].

In Figure 3a we compare the spatial profiles of θ at $t = 40$. It can be seen that the profiles inside the reaction zone are very similar. In particular, inside this zone θ rises smoothly from 0 to 1 due to the heat release from the polymerization reactions. On the other hand, the two profiles exhibit a small phase difference; in other words, the location of the front in our simulations is slightly more advanced than in [30]. This is mainly due to small differences in the initial temperature profile and in the grid resolution. An additional contributing factor is that our simulations required estimated parameters for

the solid polymer, such as thermal conductivity and heat capacity, whereas [30] employed a single-phase model and therefore did not involve any such parameters.

Figure 3b shows the spatial profiles of the initiator J at $t = 40$ as well. Ahead of the front, in the unreacted liquid mixture, J is constant and equal to unity. The elevated temperature behind the front leads to rapid consumption of the initiator. As with θ, the spatial distribution of J is very similar in the two computations, even though in ours the front is slightly more advanced.

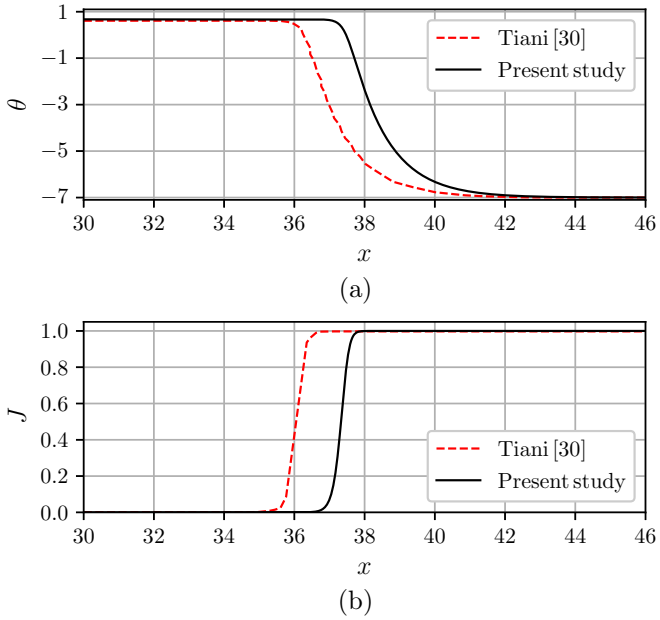


Figure 3: Case 1: spatial profiles (a) dimensionless temperature θ, and (b) dimensionless initiator concentration J at $t = 40$. The solid line corresponds to profiles obtained with the reduced RD model of the present study.

5. Numerical results obtained with the full model

In this section, we present numerical results obtained with the full two-phase model (58)–(62), and compare them with those obtained with the reduced RD model (68)–(72). Two cases are considered herein. The first one is case 1 that was described previously and corresponds to a stable front propagating with constant speed. In contrast, case 2 is an example of an unstable front.

As mentioned before, the full model assumes that the density $\rho_{\rm s}$ of the solid phase is constant, while that of the liquid, ρ, is temperature-dependent. In the present study, the liquid density is given by the following relation

$$\rho \;=\; \frac{\rho_{\rm ref}}{1+\alpha(T-T_{\rm ref})}\,, \tag{78}$$

where $\rho_{\rm ref}$ is the liquid density at the reference temperature, and α is the thermal expansion coefficient of the liquid phase. In both cases presented herein, $\alpha = 3\times10^{-4}$ K^{-1}. Also, the density of the solid phase is estimated at $\rho_{\rm s} = 1.1\rho_{\rm ref}$, whereas in the reduced RD model, the densities of both phases are constant and equal to $\rho_{\rm ref}$.

5.1. Case 1 (stable front)

This case was described in the previous section and corresponds to a stable front. Next, we compare the results obtained with the full model (which takes into account fluid motion) with the predictions of the reduced RD model.

With regard to the kinematic boundary conditions, zero velocity is prescribed at the heated wall at the left and a convective condition at the right boundary located at $x = L$. The latter allows for the exit of flow structures without spurious reflections and reads

$$\frac{\partial u_{\rm b}}{\partial t} + u_{\rm b}\frac{\partial u_{\rm b}}{\partial x} \;=\; 0\,, \tag{79}$$

where $u_{\rm b}$ denotes the liquid velocity at the right boundary. This equation is solved numerically using the method of characteristics.

Figure 4 shows the temporal evolution of the front speed, obtained with the full and reduced RD models. The polymerization front initially undergoes a rapid acceleration, resulting in a brief overshoot of the front speed before it relaxes toward a steady propagation regime. This transient overshoot is observed in both the reduced RD model and the full model. From these plots, it is inferred that both models predict the same transient stage that leads to the establishment of the polymerization front. Moreover, the terminal front speed is attained at the same time. The only visible difference is that, globally, the steady-state front speed predicted by the full model is slightly inferior to that computed via the reduced RD model, specifically, it is 8.77% lower. In other words, fluid motion leads to lower front speed.

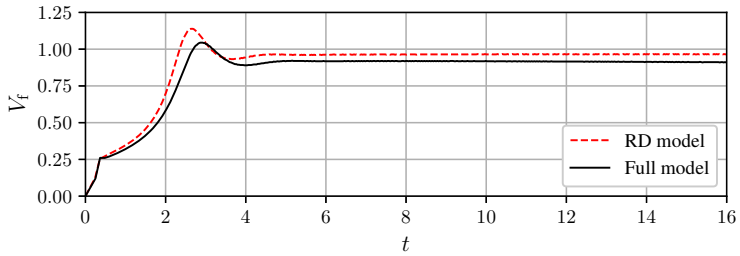


Figure 4: Case 1: Temporal evolution of the front speed V_f. The solid line corresponds to the full model ($u \neq 0$), whereas the dashed line corresponds to the reduced RD model ($u = 0$).

In Figures 5a and 5b we have plotted the profiles of the dimensionless temperature θ at two different time instances, $t = 20$ and $t = 40$. We observe that the profiles are very similar. Nonetheless, the profile predicted by the full model lags behind that of the reduced RD model. This is due to the fact that the front speed computed with the full model is slightly lower. Accordingly, this lag increases slowly but steadily with time.

The same observations also hold for the profiles of the dimensionless initiator concentration J, shown in Figures 5c and 5d. Further, in these plots, it is interesting to observe that in the early stages of the polymerization, the profile of J predicted with the full model is smoother than that predicted with the reduced RD model. In other words, fluid motion contributes to lower consumption rates of the initiator in the early stages of the process.

Next, in Figure 6 we present spatial profiles of the liquid volume fraction ϕ, at $t = 20$ and $t = 40$. The sharp transition region in the bulk of the domain corresponds to the reaction zone that separates the unreacted liquid and the polymerized material. We further observe that the liquid volume fraction behind the front does not vanish, even though the initiator has been fully consumed. In other words, the conversion to polymer is not complete and there is a substantial concentration of monomer behind the front. This further implies that the final material is rather a porous solid polymer with monomer filling up its voids. In this particular case the monomer volume fraction behind the front is quite high. The incomplete conversion can be attributed to the high temperature inside the reaction zone, which leads to rapid initiator consumption, hence low radical concentration, by virtue of the steady-state approximation (56). This implies lower availability of radicals to participate in the propagation reaction (48) and, in turn, results

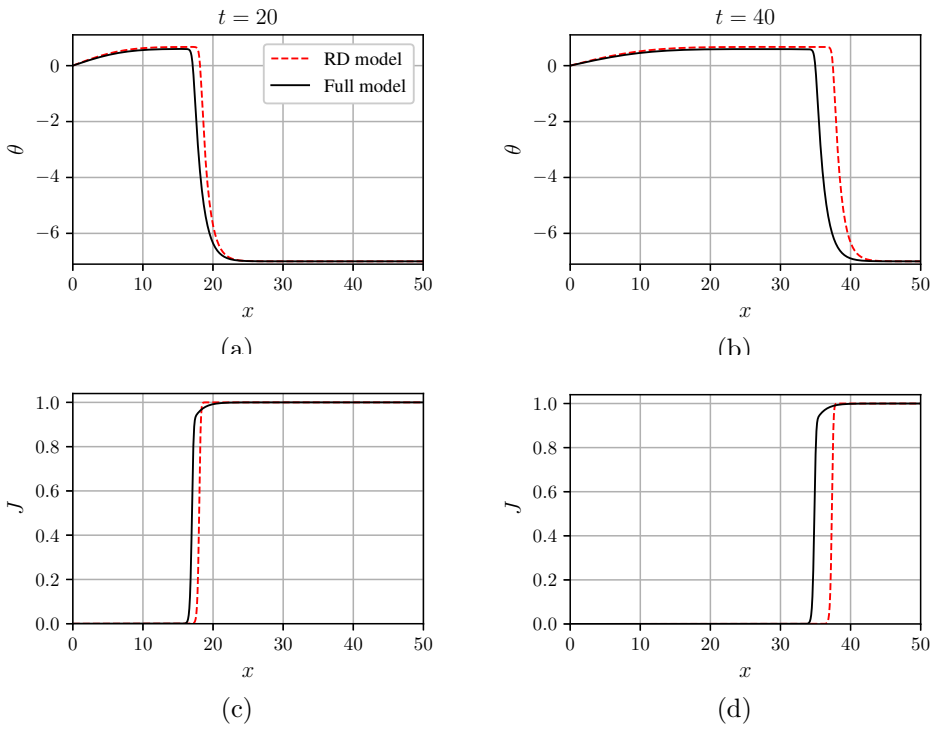


Figure 5: Case 1: Spatial profiles of the dimensionless temperature θ (a,b) and the dimensionless initiator concentration J (c,d) at two different time instances. The solid lines correspond to the full model ($u \neq 0$), whereas the dashed lines correspond to the RD model ($u = 0$).

in incomplete monomer consumption. Incomplete conversion and persistence of unreacted monomer behind propagating fronts is not uncommon; see, for example, [8] for an experimental study and relevant discussion.

It is also important to note that there is a noticeable difference in the value of ϕ behind the polymerization front. More specifically, the reduced RD model predicts $\phi \approx 0.7$ whereas the full model predicts that $\phi \approx 0.62$. In other words, even though fluid motion only mildly affects the front speed, it results in noticeably lower conversion and larger amounts of unreacted monomer in the final product.

Finally, in Figure 7 we present plots of the spatial profiles of the liquid velocity at various time instances. These plots show that in most of the reaction zone and in the entire region behind the front, the liquid velocity is negative. This is due to the shrinkage associated with polymerization. More

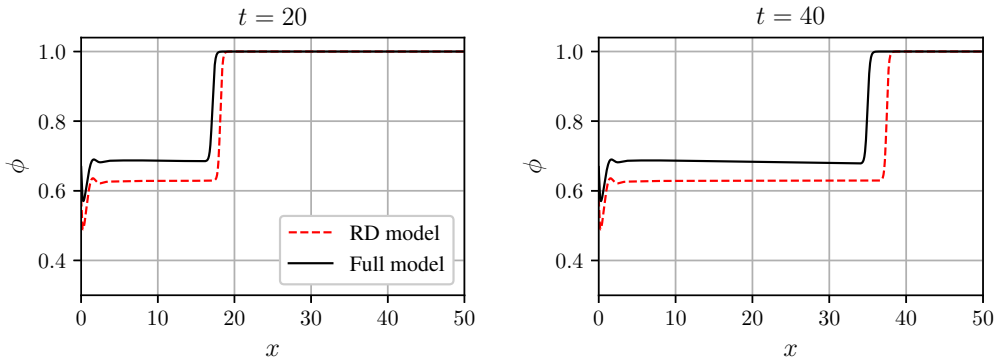


Figure 6: Case 1: Spatial profiles of the liquid volume fraction ϕ at two time instances, $t = 20$ and $t = 40$. The sharp transition region in the bulk of the domain corresponds to the reaction zone, which separates the unreacted liquid from the polymerized material.

specifically, the solid phase is denser than the liquid $\rho_s > \rho$, and therefore the conversion to solid polymer leads to the availability of space that is filled by the liquid. In other words, the volumetric contraction due to polymerization induces fluid motion toward the solid polymer (to the left).

On the other hand, in the early stage of the polymerization process, the opposite phenomenon occurs. In this stage, the dominant phenomenon is the preheating of the liquid reactants while the conversion to solid polymer is still low. Then, as the liquid becomes hotter, it expands, which results in the formation of a local negative pressure gradient. This, in turn, causes the unreacted liquid to move in the same direction as the front. The liquid velocity ahead of the front is rather small, albeit nonzero. Further, the liquid velocity decreases as the exit boundary is approached. More specifically, at that boundary, the liquid velocity practically vanishes.

5.2. Case 2: unstable front

In this case the front is subject to chemical instabilities that give rise to significant fluctuations of the front speed and species concentrations. Herein we use the same parameters as those in a similar case studied in [11] which exhibited one unstable mode and oscillatory front behavior. The study in [11] was based on a single-phase reaction-diffusion model and a three-step reaction mechanism. However, in our study we had to employ estimates for the molar masses and the thermophysical properties of the solid phase, since those are not mentioned in [11]. Consequently, it is not possible to reproduce

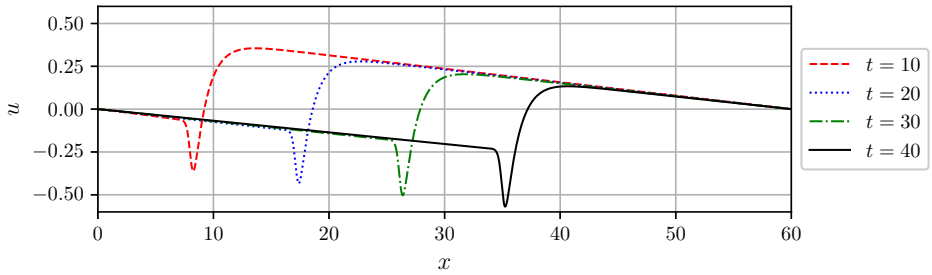


Figure 7: Case 1: profiles of the dimensionless liquid velocity at different time instances, computed with the full model.

exactly the same case as in [11]. With the given choice of our estimates, our simulations predicted that this case is subject to a multitude of unstable modes, Further, in our simulations we observed extreme sensitivity of the front evolution to the initial conditions. Such behavior is typical of systems with many unstable modes and may suggest chaotic front dynamics.

The initial setup is similar to that of case 1, with the exception that now the initial concentration of the initiator is $Y_{\mathrm{I}} = 0.0047$, and $T_{\mathrm{i}} = 490$ K. Also, the boundary conditions are the same as case 1, except that an adiabatic (zero-Neumann) boundary condition is prescribed at the left boundary for T. Then, the front is developed with the aid of energy supply, in the form of heat added to a small portion of the liquid solution adjacent to the left boundary. The values of the parameters and constants for this case are provided in Table 2. The computational domain has a length $L = 20$ cm and is discretized into $n = 2000$ uniform computational segments.

Results for the temporal evolution of the front speed, obtained by the full model and the reduced RD model, are provided in Figure 8. Therein we observe that the front speed exhibits large fluctuations and is further characterized by large overshoots that are preceded by long periods of very slow (almost vanishing) front advancement. This behavior is reminiscent of low-dimensional [36, 37]; such systems are aperiodic, extremely sensitive to initial data, and bounded.

We further observe that, qualitatively, the predictions of both models are very similar. Nonetheless, the average front speed predicted with the full model is slightly inferior to that predicted with the reduced RD model. This, however, does not imply that fluid motion always results in a small decrease of the front speed. As a matter of fact, in the context of our study,

Variable	Value	Variable	Value
ρ_{ref}	1038 kg/m^3	k^0_{eff}	8.16×10^9 m$^{3/2}$/(s mol$^{1/2}$)
f	0.5	k^0_{d}	4×10^{12} 1/s
T_0	292 K	k^0_{p}	1×10^6 m^3/(s.mol)
T_{a}	490 K	k^0_{t}	3×10^4 m^3/(s.mol)
T_{i}	490 K	E_{d}	1.255×10^5 J/mol
l_{ref}	8×10^{-4} m	E_{p}	4.393×10^4 J/mol
t_{ref}	4.522 s	E_{t}	2928.8 J/mol
η_{ref}	1.5×10^{-3} Pa s	E_{eff}	1.052×10^5 J/mol
c_p	1673.6 J/(kg K)	$c_{\mathrm{I}}(0)$	20 mol/m^3
c_{s}	1506.2 J/(kg K)	$c_{\mathrm{M}}(0)$	6000 mol/m^3
κ	0.243 W/(m K)	M_{I}	0.242 kg/mol
κ_{s}	0.209 W/(m K)	M_{M}	0.172 kg/mol
α	3×10^{-4} 1/K	$h^{\mathrm{f}}_{\mathrm{M}}$	5.774×10^4 J/mol

Table 2: Case 2: values of the various parameters and constants.

we observed that in some cases fluid motion led to the increase of the front speed.

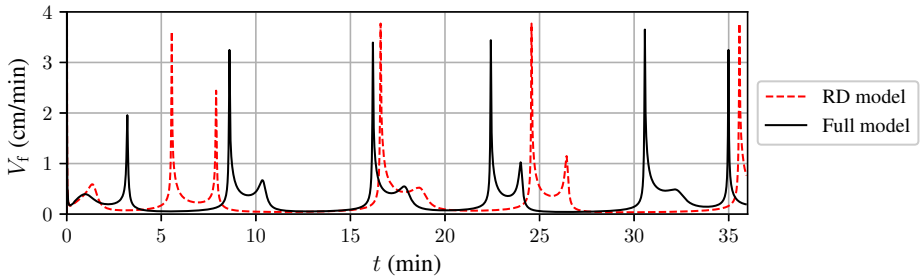


Figure 8: Case 2: temporal evolution of the front speed V_{f}. The solid line corresponds to the result obtained with the full model ($u \neq 0$), whereas the dashed line corresponds to that obtained with the reduced RD model ($u = 0$). The average front speed predicted with the full model is slightly inferior to that predicted with the reduced RD model.

It is worth noting that the temporal evolution of the front speed is strikingly similar to that of unstable gaseous detonation waves [38–41], even though the front speeds in TFP and detonations differ by more than 6 orders of magnitude. This has been already acknowledged before [11] and is due to the intrinsic instabilities of exothermic chain reaction mechanisms governed by Arrhenius kinetics laws. In other words, TFP and gaseous detonations have similar reaction mechanisms and are subject to the same instabilities.

Figure 9 displays plots of the spatial profiles of the temperature at dif-

ferent time instances. We observe that these profiles are non-monotonic but exhibit fluctuations behind the front. These are due to the irregular heat release that is characterized by large bursts and rapid conversion, preceded by long periods of slow conversion and low heat-release rates. In other words, as the front speed fluctuates due to chemical instabilities, so do the spatial profiles of the various variables behind the front. This behavior is predicted by both models. Evidently, pointwise comparisons of the instantaneous profiles are not meaningful due to the highly unstable behavior of the system at hand.

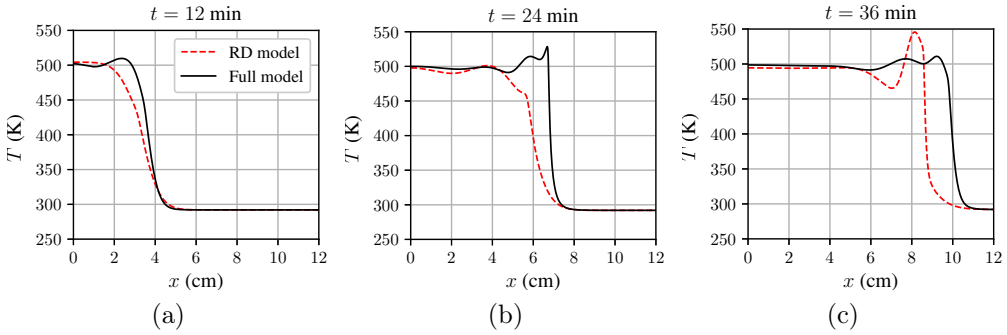


Figure 9: Case 2: spatial profiles of the temperature T at different time instances.

Figures 10a and 10b depict profiles of the monomer concentration c_{M} at two time instances. We observe that behind the front there is always some monomer, which signals incomplete conversion. Moreover, the monomer concentration behind the front fluctuates substantially. In particular, there are regions in which the monomer concentration is almost zero and others where it is 25% of the initial value. This, in turn, implies that the final product is not homogeneous and displays large spatial inhomogeneities, which can have an impact on its mechanical and thermal properties. It is also interesting to note that, overall, the full model and the reduced RD one predict the same levels of monomer conversion behind the front.

The fluctuations of the monomer concentration are due to the highly unstable behavior of the front. Actually, they constitute "traces" of the variations of the front speed in the following sense. When the front speed V_{f} peaks suddenly, there is a large amount of heat is released in a short time, leading to very rapid consumption of initiator and thus radicals. This leads to a local deficit of radicals to react with the monomer in the propagation step, hence large monomer concentrations. In fact, the local peaks of c_{M}

behind the front correspond to the (spatial) locations where the front speed has reached a sharp peak.

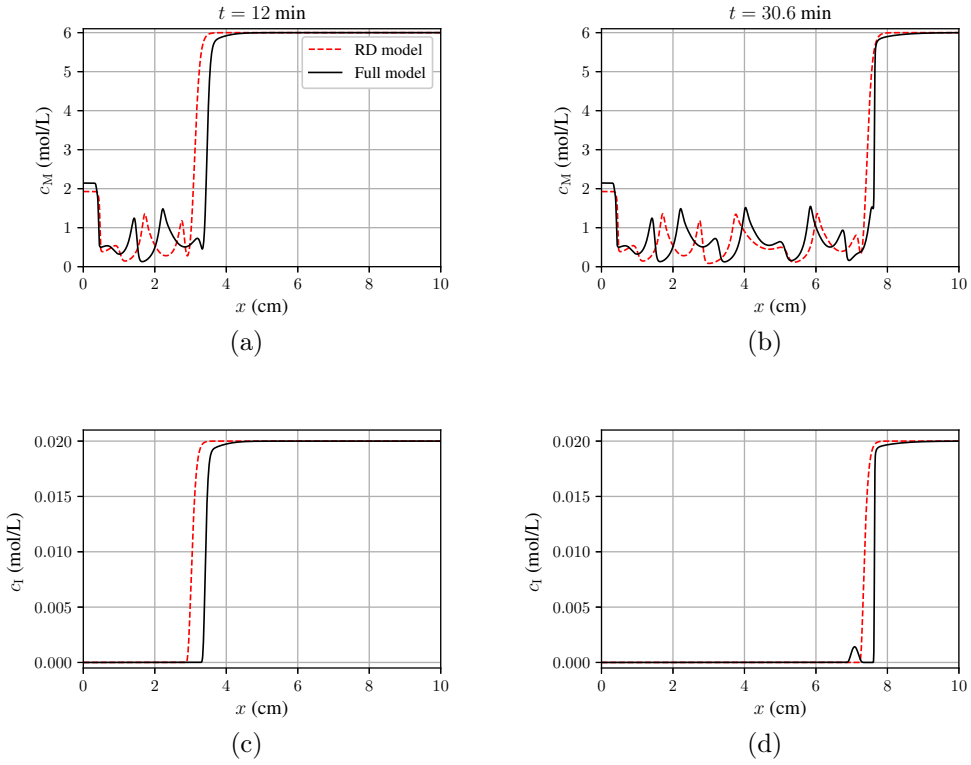


Figure 10: Case 2: spatial profiles of the monomer concentration c_M, (a,b) and initiator concentration c_I (c,d) at two different time instances. In (d), and in the profile obtained with the full model, we can observe the presence of a pocket of unconsumed initiator.

Further, in Figures 10c and 10d we provide plots of the spatial profiles of the initiator concentration, c_I, at two different time instances. We observe that the initiator is consumed very rapidly despite the instabilities of the front. Also, as in case 1, the full model predicts a smoother initiator consumption in the early stage of the polymerization process.

However, and in contrast to case 1, both models predict that, in certain instances, there are small pockets of unconsumed initiator behind the front. Such a pocket of unreacted initiator is shown in Figure 10d. These pockets are formed due to the front instabilities but are consumed quite rapidly because of the high temperature. Their consumption constitutes a secondary polymerization process behind the main front. Similar behavior of pockets

of partially unreacted material is also typical of highly unstable gaseous detonations [38]. Another minor difference from case 1 is that the gradient of c_{I} is no longer constant. It remains steep but fluctuates with time. In other words, the consumption rate of the initiator is not constant but exhibits variations due to the instabilities of the front.

Finally, in Figure 11 we present plots of the liquid velocity profiles, as predicted by the full model. We readily observe that these profiles have opposite trends to those in case 1, which was a stable case. More specifically, ahead of the front the liquid velocity is negative, which means that the liquid goes toward the front, whereas behind the front the monomer residue attains a very small positive velocity, i.e. it moves toward the front as well. This is due to two reasons. The first one is that the overall conversion of monomer behind the front is higher than in case 1. The second one is that, because of the irregular advancement of the front, the rate of volumetric contraction inside the reaction zone varies wildly with time. Accordingly, when the front advances at high speeds, the conversion to polymer becomes very rapid and so does the volumetric contraction rate. This implies that liquid monomer is driven toward the front. But behind the front there is a much smaller amount of residual monomer and this amount is also subject to interfacial drag. Accordingly, most of the monomer that fills the space generated by polymerization is initially located ahead of the front. In a sense, the rapid volumetric contraction creates an adverse pressure gradient ahead of the front that drives the liquid solution toward the reaction zone. It is also worth observing that the magnitudes of the velocity extrema, which are located inside the reaction zone, vary with time according to the fluctuations of the front.

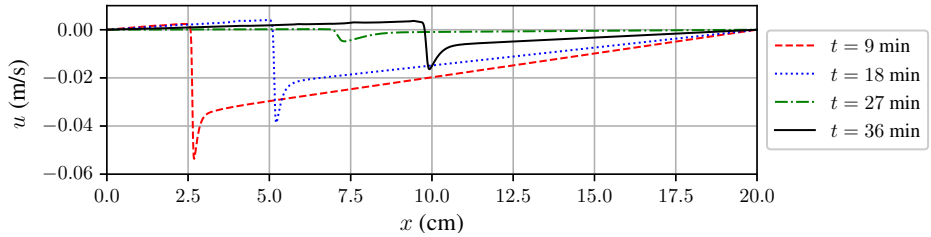


Figure 11: Case 2: spatial profiles of the liquid velocity at different time instances.

6. Conclusions

In this paper, we presented a novel thermo-mechanical two-phase model for TFP, which takes into account fluid motion and related hydrodynamic effects. It is based on a unified mixture-theoretic framework that treats the liquid reactants and solid polymer as interacting continua that coexist in space. By integrating chemical kinetics for both homogeneous and heterogeneous reactions, heat transfer, and hydrodynamic effects, this approach overcomes certain limitations of previous single-phase models. This model, and the corresponding algorithm for its numerical treatment, have been validated via comparisons with previously published numerical results and numerical convergence studies.

Further, we presented results from simulations of two case studies, one stable and one unstable. According to these results, fluid motion impacts the monomer conversion and, to a lesser extent, the average front speed. Also, fluid motion is driven by volumetric contraction (the solid polymer is denser than the initial liquid solution) that drives the monomer solution toward the reaction zone. Additionally, our numerical investigations confirmed that for a wide range of parameters, the polymerization front is subject to chemical instabilities, leading to unstable front dynamics.

Acknowledgements

The authors gratefully acknowledge funding from FRS-FNRS (T.W009.23) and FWO under the WEAVE Project G0A3723N.

Appendix A. A time-accurate algorithm of two-phase modeling of thermal frontal polymerization

Below we present a time-accurate algorithm from the numerical treatment of the two-phase TFP model developed in this paper. It employs a predictor–corrector time-integration scheme, combined with a projection method for the computation of the pressure. In regions with large temperature gradients, the gravity term can vary substantially. In such cases, for purposes of computational stability and efficiency, it is useful to cast the momentum equation in terms of the piezometric pressure. In order to fix ideas let us assume that the gravitational acceleration is parallel to the y direction. Then, the piezometric pressure reads $p' = p + \rho g y$, with g being the magnitude of $\boldsymbol{g}$. The algorithm consists of the following steps.

Appendix A.1. Predictor

In the predictor stage, estimates of the field variables at the next timestep are obtained by performing a first time integration of the governing system.

i) The predicted value for the temperature, T^*, is calculated from equation (62), based on the values from the previous timestep n,

$$\left(\phi\rho c_p + \phi_\mathrm{s}\rho_\mathrm{s}c_\mathrm{s}\right)^n \frac{T^* - T^n}{\Delta t} = \frac{1}{2}\left(3Res_T^n - Res_T^{n-1}\right) , \tag{A.1}$$

with Res_T is given by

$$\begin{aligned} Res_T \;=\; & -\phi\rho c_p \boldsymbol{u}\cdot\nabla T - \nabla\cdot\left(\phi\boldsymbol{q} + \phi_\mathrm{s}\boldsymbol{q}_\mathrm{s}\right) - h_\mathrm{M}^\mathrm{f}\dot{\omega}_\mathrm{M}' M_\mathrm{M} \\ & - \mathcal{M}\left(\left(c_p - c_\mathrm{s}\right)\left(T - T_\mathrm{ref}\right) - \frac{p^0}{\rho_\mathrm{s}}\right) . \end{aligned} \tag{A.2}$$

ii) The temperature-dependent variables are updated, so the predicted value for the density, ρ^*, is calculated from equation (78).

iii) The predicted value for the initiator mass fraction, Y_I^*, is calculated from equation (59), based on the values from the previous timestep n,

$$\left(\phi\rho\right)^n \frac{Y_\mathrm{I}^* - Y_\mathrm{I}^n}{\Delta t} \;=\; \frac{1}{2}\left(3Res_Y^n - Res_Y^{n-1}\right) . \tag{A.3}$$

with Res_Y is given by

$$Res_Y \;=\; -\phi\rho\boldsymbol{u}\cdot\nabla Y_\mathrm{I} + \dot{\omega}_\mathrm{I}' M_\mathrm{I} - \mathcal{M}Y_\mathrm{I} . \tag{A.4}$$

iv) The predicted value for the fluid volume fraction, ϕ^*, is calculated from equation (61),

$$\frac{\phi^* - \phi^n}{\Delta t} \;=\; \frac{1}{\rho_\mathrm{s}}\mathcal{M}^n . \tag{A.5}$$

v) A provisional velocity, $\tilde{\boldsymbol{u}}$, is introduced as the solution of the momentum equation (60) without the pressure term and the body force. The component of the viscous flux in the gravity direction and the drag term are integrated in time via the semi-implicit Crank–Nicolson method, while all other terms are integrated in time explicitly via the Adams

Bashforth method. This strategy yields computationally efficient tridiagonal systems while maintaining stability.

$$\frac{(\rho\phi)^* \tilde{\boldsymbol{u}} - (\rho\phi\boldsymbol{u})^n}{\Delta t} = \frac{1}{2}\left(3Res_{\boldsymbol{u}}^n - Res_{\boldsymbol{u}}^{n-1}\right) - \frac{1}{2}\left(\widetilde{\boldsymbol{u}} + \boldsymbol{u}^n\right)\delta^n + \frac{1}{2}\widetilde{\mathbf{c}}\frac{\partial}{\partial y}\left((\phi\eta)^* \frac{\partial \widetilde{\boldsymbol{u}}}{\partial y} + (\phi\eta)^n \frac{\partial \boldsymbol{u}^n}{\partial y}\right), \tag{A.6}$$

with $\widetilde{\mathbf{c}} = \mathrm{diag}\left(1, \frac{4}{3}, 1\right)$. The components of $Res_{\boldsymbol{u}}$ are as follows

$$Res_u = -\nabla\cdot(\phi\rho\boldsymbol{u}u) + \left[\frac{\partial}{\partial x}\left(\phi\eta\left(2\frac{\partial u}{\partial x} - \frac{2}{3}\nabla\cdot\boldsymbol{u}\right)\right) + \frac{\partial}{\partial y}\left(\phi\eta\frac{\partial v}{\partial x}\right) + \frac{\partial}{\partial z}\left(\phi\eta\left(\frac{\partial u}{\partial z} + \frac{\partial w}{\partial x}\right)\right)\right], \tag{A.7}$$

$$Res_v = -\nabla\cdot(\phi\rho\boldsymbol{u}v) + \left[\frac{\partial}{\partial x}\left(\phi\eta\left(\frac{\partial u}{\partial y} + \frac{\partial v}{\partial x}\right)\right) - \frac{2}{3}\frac{\partial}{\partial y}\left(\phi\eta\left(\frac{\partial u}{\partial x} + \frac{\partial w}{\partial z}\right)\right) + \frac{\partial}{\partial z}\left(\phi\eta\left(\frac{\partial v}{\partial z} + \frac{\partial w}{\partial y}\right)\right)\right], \tag{A.8}$$

$$Res_w = -\nabla\cdot(\phi\rho\boldsymbol{u}w) + \left[\frac{\partial}{\partial x}\left(\phi\eta\left(\frac{\partial u}{\partial z} + \frac{\partial w}{\partial x}\right)\right) + \frac{\partial}{\partial y}\left(\phi\eta\frac{\partial v}{\partial z}\right) + \frac{\partial}{\partial z}\left(\phi\eta\left(2\frac{\partial w}{\partial z} - \frac{2}{3}\nabla\cdot\boldsymbol{u}\right)\right)\right]. \tag{A.9}$$

vi) By taking the divergence of the momentum balance equation (60) and substituting the mass balance relations (58) and (61), we obtain a linear elliptic equation for the pressure,

$$\nabla\cdot\left(\phi^*\nabla p'^*\right) = \frac{1}{\Delta t}\nabla\cdot\left((\rho\phi)^*\tilde{\boldsymbol{u}}\right) - \frac{1}{\Delta t}\mathcal{M}^*\frac{\rho_{\mathrm{s}} - \rho^*}{\rho_{\mathrm{s}}} + \phi^*\frac{3\rho^* - 4\rho^n + \rho^{n-1}}{2\Delta t^2} + g\nabla\cdot(\phi^* y\nabla\rho^*). \tag{A.10}$$

The predicted value of the piezometric pressure, p'^* is calculated by discretizing and solving numerically this equation.

vii) Once the pressure is computed, the predicted values of the velocity field $\boldsymbol{u}^*$ are calculated by going back ot the momentum equation, via

$$\boldsymbol{u}^* = \tilde{\boldsymbol{u}} - \frac{\Delta t}{\rho^*}\left(\nabla p'^* - gy\nabla\rho^*\right). \tag{A.11}$$

Appendix A.2. Corrector

In the corrector stage, the field variables are updated to the next timestep $n+1$, following the same sequence of steps that was described in detail for the predictor step.

i) The corrected value for the temperature, T^{n+1}, is calculated from equation (62),

$$\left(\phi\rho c_p + \phi_{\mathrm{s}}\rho_{\mathrm{s}}c_{\mathrm{s}}\right)^* \frac{T^{n+1}-T^n}{\Delta t} \;=\; \frac{1}{2}\left(Res_T^* + Res_T^n\right) . \tag{A.12}$$

ii) The temperature-dependent variables are updated, so the corrected value for the density, ρ^{n+1}, is calculated from equation (78).

iii) The corrected value for the initiator mass fraction, Y_{I}^{n+1}, is calculated from equation (59),

$$\left(\phi\rho\right)^* \frac{Y_{\mathrm{I}}^{n+1}-Y_{\mathrm{I}}^n}{\Delta t} \;=\; \frac{1}{2}\left(Res_Y^* + Res_Y^n\right) . \tag{A.13}$$

iv) The corrected value for the fluid volume fraction, ϕ^{n+1}, is calculated from equation (61),

$$\frac{\phi^{n+1}-\phi^n}{\Delta t} \;=\; \frac{1}{\rho_{\mathrm{s}}}\mathcal{M}^* . \tag{A.14}$$

v) The intermediate velocity, $\widehat{\boldsymbol{u}}$, is calculated from the momentum equation (60),

$$\begin{aligned}\frac{\left(\rho\phi\right)^{n+1}\widehat{\boldsymbol{u}} - \left(\rho\phi\boldsymbol{u}\right)^n}{\Delta t} \;&=\; \frac{1}{2}\left(Res_{\boldsymbol{u}}^* + Res_{\boldsymbol{u}}^n\right) - \frac{1}{2}\left(\widehat{\boldsymbol{u}} + \boldsymbol{u}^n\right)\delta^* \\ &\quad + \frac{1}{2}\widetilde{\mathbf{c}}\,\frac{\partial}{\partial y}\left(\left(\phi\eta\right)^{n+1}\frac{\partial\widehat{\boldsymbol{u}}}{\partial y} + \left(\phi\eta\right)^n\frac{\partial\boldsymbol{u}^n}{\partial y}\right) .\end{aligned} \tag{A.15}$$

vi) The corrected value of the piezometric pressure, p'^{n+1}, is computed by solving the following linear elliptic equation, which results by taking the divergence of the momentum equation,

$$\begin{aligned}\nabla\cdot\left(\phi^{n+1}\nabla\left(p'\right)^{n+1}\right) \;&=\; \frac{1}{\Delta t}\nabla\cdot\left(\left(\rho\phi\right)^{n+1}\widehat{\boldsymbol{u}}\right) - \frac{1}{\Delta t}\,\mathcal{M}^{n+1}\,\frac{\rho_{\mathrm{s}}-\rho^{n+1}}{\rho_{\mathrm{s}}} \\ &\quad + \phi^{n+1}\frac{3\rho^{n+1}-4\rho^n+\rho^{n-1}}{2\Delta t^2} \\ &\quad + g\nabla\cdot\left(\phi^{n+1}y\nabla\rho^{n+1}\right) .\end{aligned} \tag{A.16}$$

vii) Finally, the corrected values of the velocity field $\boldsymbol{u}^{n+1}$ are directly calculated as

$$\boldsymbol{u}^{n+1} \;=\; \widehat{\boldsymbol{u}} - \frac{\Delta t}{\rho^{n+1}} \left(\nabla \left(p' \right)^{n+1} - gy \nabla \rho^{n+1} \right). \tag{A.17}$$

References

[1] A. G. Merzhanov, I. P. Borovinskaya, Self-propagating high-temperature synthesis of refractory inorganic compounds, Dokl. Akad. Nauk 204 (2) (1972) 366–369.

[2] N. M. Chechilo, R. Y. Khvilivitsky, N. S. Enikolopyan, The phenomenon of propagation of the polymerization reaction, Dokl. Phys. Chem. 204 (1972) 512–513.

[3] N. M. Chechilo, N. S. Enikolopyan, Structure of the polymerization wave front and propagation mechanism of the polymerization reaction, Dokl. Phys. Chem. 214 (5) (1974) 174–176.

[4] N. M. Chechilo, N. S. Enikolopyan, Effect of the concentration and nature of initiators on the propagation process in polymerization, Dokl. Phys. Chem. 221 (5) (1975) 392–394.

[5] N. M. Chechilo, N. S. Enikolopyan, Effect of pressure and initial temperature of the reaction mixture during propagation of a polymerization reaction, Dokl. Phys. Chem. 230 (1976) 840–843.

[6] J. A. Pojman, V. Ilyashenko, A. M. Khan, Free-radical frontal polymerization: Self-propagating thermal reaction waves, J. Chem. Soc., Faraday Trans. 92 (1996) 2825–2837.

[7] J. A. Pojman, R. Craven, A. Khan, W. West, Convective instabilities in traveling fronts of addition polymerization, J. Phys. Chem. 96 (18) (1992) 7466–7472.

[8] J. A. Pojman, J. Willis, D. Fortenberry, V. Ilyashenko, A. M. Khan, Factors affecting propagating fronts of addition polymerization: Velocity, front curvature, temperature profile, conversion, and molecular weight distribution, J. Polym. Sci., Part A: Polym. Chem. 33 (4) (1995) 643–652.

[9] J. A. Pojman, Mathematical modeling of frontal polymerization, Math. Modell. Nat. Phenom. 14 (6) (2019) 604.

[10] J. A. Pojman, Frontal polymerization, in: K. Matyjaszewski, M. Möller (Eds.), Polymer Science: A Comprehensive Reference, Vol. 4, Elsevier, Amsterdam, 2012, pp. 957–980.

[11] S. E. Solovyov, V. M. Ilyashenko, J. A. Pojman, Numerical modeling of self-propagating polymerization fronts: The role of kinetics on front stability, Chaos 7 (1997) 331–340.

[12] C. A. Spade, V. A. Volpert, Linear stability analysis of non-adiabatic free-radical polymerization waves, Combust. Theory Modell. 5 (1) (2001) 21.

[13] A. Heifetz, L. R. Ritter, W. E. Olmstead, V. A. Volpert, A numerical analysis of initiation of polymerization waves, Math. Comput. Modell. 41 (2) (2005) 271–285.

[14] R. Texier-Picard, J. A. Pojman, V. A. Volpert, Effect of interfacial tension on propagating polymerization fronts, Chaos 10 (1) (2000) 224–230.

[15] T. Dumont, Numerical simulation of frontal polymerization, Comput. Assist. Methods Eng. Sci. 7 (3) (2000) 363–376.

[16] Y. Gao, S. Li, J.-Y. Kim, I. Hoffman, S. K. Vyas, J. A. Pojman, P. H. Geubelle, Anisotropic frontal polymerization in a model resin–copper composite, Chaos 32 (1) (2022) 013109.

[17] Y. Gao, F. Shaon, A. Kumar, S. Bynum, D. Gary, D. Sharp, J. A. Pojman, P. H. Geubelle, Rapid frontal polymerization achieved with thermally conductive metal strips, Chaos 31 (7) (2021) 073113.

[18] R. Tiani, J. A. Pojman, L. Rongy, Critical role of layer thickness in frontal polymerization, J. Phys. Chem. B 126 (19) (2022) 3607–3618.

[19] T. P. Ivleva, A. G. Merzhanov, Three-dimensional modes of unsteady solid-flame combustion, Chaos 13 (1) (2003) 80–86.

[20] E. Goli, N. A. Parikh, M. Yourdkhani, N. G. Hibbard, J. S. Moore, N. R. Sottos, P. H. Geubelle, Frontal polymerization of unidirectional carbon-fiber-reinforced composites, Composites, Part A 130 (2020) 105689.

[21] X. Yi, S. Li, P. Wen, S. Yan, Numerical simulation of polyacrylamide hydrogel prepared via thermally initiated frontal polymerization, Polymers 16 (873) (2024).

[22] W. Yan, R. Liu, C. Fowler, S. Wang, J. Qiu, Multiphysics modeling of frontal curing-enabled additive manufacturing for carbon fiber/thermoset composites, Comput. Mater. Sci. 237 (2024) 112916.

[23] Y. Gao, J. E. Paul, M. Chen, L. Hong, L. P. Chamorro, N. R. Sottos, P. H. Geubelle, Buoyancy-induced convection driven by frontal polymerization, Phys. Rev. Lett. 130 (2023) 028101.

[24] M. Lang, C. Schmidleitner, V. P. Kasinikota, E. Rossegger, Thermal frontal polymerization in polymer composites: Numerical simulation and the role of Fe_3O_4 nanoparticle fillers, Appl. Compos. Mater. 32 (2025) 1025–1045.

[25] L. Rongy, P. Assemat, A. De Wit, Marangoni-driven convection around exothermic autocatalytic chemical fronts in free-surface solution layers, Chaos 22 (3) (2012) 037106.

[26] M. V. Papalexandris, P. D. Antoniadis, A thermo-mechanical model for flows in superposed porous and fluid layers with interphasial heat and mass exchange, Int. J. Heat Mass Transfer 88 (2015) 42–54.

[27] S. R. de Groot, P. Mazur, Non-equilibrium Thermodynamics, Dover, 1984.

[28] D. K. Kondepundi, I. Prigogine, Modern thermodynamics: from Heat Engines to Dissipative Structures, Wiley, 1998.

[29] C. Varsakelis, M. V. Papalexandris, Low-Mach-number asymptotics for two-phase flows of granular materials, J. Fluid Mech. 669 (2011) 472–497.

[30] R. Tiani, Dynamics of chemical fronts driven by reaction-diffusion processes and convective effects, Ph.D. thesis, Université Libre de Bruxelles (2021).

[31] M. V. Papalexandris, Boundary-layer flow in a porous domain above a flat plate, J. Eng. Math. 140 (2023).

[32] B. Lessani, M. V. Papalexandris, Time-accurate calculation of variable density flows with strong temperature gradients and combustion, J. Comput. Phys. 212 (2006) 218–246.

[33] P. D. Antoniadis, M. V. Papalexandris, Numerical study of unsteady, thermally-stratified shear flows in superposed porous and pure-fluid domains, Int. J. Heat Mass Transfer 96 (2016) 643–659.

[34] V. Hamtiaux, M. V. Papalexandris, Turbulent thermal convection in mixed porous-pure fluid domains, J. Fluid Mech. 961 (2023) A27.

[35] J. Carlier, M. V. Papalexandris, Natural convection in an evaporative air-water system inside a cavity heated by an immersed porous medium, Phys. Fluids 37 (2025) 125193.

[36] G. Nicolis, Introduction to Nonlinear Science, Cambridge University Press, Cambridge, 1995.

[37] A. Lasota, M. C. Mackey, Chaos, Fractals, and Noise: Stochastic Aspects of Dynamics, Springer New York, 1994.

[38] M. V. Papalexandris, A. Leonard, P. E. Dimotakis, Unsplit schemes for hyperbolic conservation laws with source terms in one space dimension, J. Comput. Phys. 134 (1) (1997) 31–61.

[39] A. Bourlioux, A. J. Majda, V. Roytburd, Theoretical and numerical structure for unstable one-dimensional detonations, SIAM J. Appl. Math. 51 (2) (1991) 303–343.

[40] H. D. Ng, M. I. Radulescu, A. J. Higgins, N. Nikiforakis, J. H. S. Lee, Numerical investigation of the instability for one-dimensional chapman–jouguet detonations with chain-branching kinetics, Combust. Theory Modell. 9 (3) (2005) 385–401.

[41] H. Ng, A. Higgins, C. Kiyanda, M. Radulescu, J. Lee, K. Bates, N. Nikiforakis, Nonlinear dynamics and chaos analysis of one-dimensional pulsating detonations, Combust. Theory Modell. 9 (1) (2005) 159–170.